Earth, Planets and Space

FULL PAPER

Open Access

Strong-motion simulation for the 1944 Tonankai earthquake based on the statistical green's function method and stochastic representation of complex source process

Eri Ito[1*], Kenichi Nakano[2], Haruko Sekiguchi[1], Fumiaki Nagashima[1] and Hiroshi Kawase[1]

Abstract

Precisely evaluating the source, path, and site terms in a broadband frequency range is indispensable for quantitatively predicting strong motions. We conducted a generalized spectral inversion of strong motion in Japan to delineate both the spectral amplitude and phase characteristics for statistical Green's functions. To predict ground motion from future megathrust earthquakes, we also need to model a kinematic source with a stochastic representation of the slip and rupture velocities on the fault surface. In this fundamental study, we first reported the basic features of statistical Green's functions used for summation. We then demonstrated the construction of a kinematic source with distinctive strong-motion-generation areas with spatially random slip and rupture velocity variations. After the summation of statistical Green's functions following the constructed kinematic source, we found that the peak ground accelerations and peak ground velocities of synthetics for the Mw8.2 1944 Tonankai earthquake are in good agreement with those of the well-established empirical formula in Japan because the medians of the synthetic values are well within the average plus/minus one standard deviation of the formula. Based on the simulation results of conducted parametric studies, we observed relatively small but meaningful effects of random slip distribution, as well as relatively small effects of random rupture velocity perturbation. In conclusion, our implementation of the complex source model and the empirically obtained statistical Green's function used as an element source can be a viable combination for broadband (0.1 to 20 Hz) strong-motion simulations, realistic in terms of the amplitude and duration, without any hybrid scheme.

Keywords 1944 Tonankai earthquake, Heterogeneous source model, Statistical Green's function

*Correspondence:
Eri Ito
ito@sere.dpri.kyoto-u.ac.jp
Full list of author information is available at the end of the article

Graphical Abstract

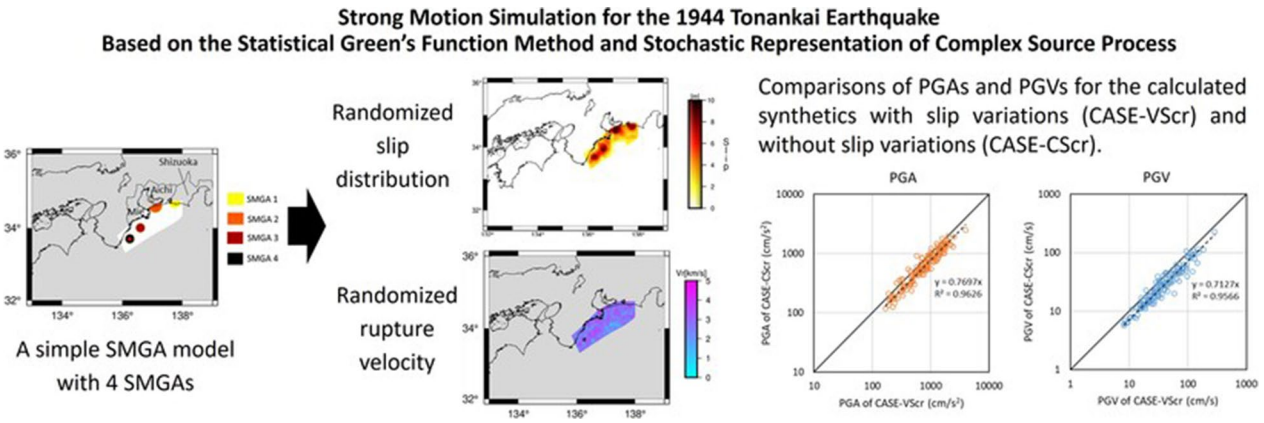

Introduction

Quantitative prediction of strong motion with source- and site-specific schemes is crucial for mitigating earthquake disasters and for the seismic design of important structures. This is especially true in Japan, where large megathrust earthquakes are expected to occur within the next 30 years along the Nankai Trough at the subduction interface between the Japanese Islands and the Philippine Sea Plate (The Headquarters for Earthquake Research Promotion 2022). Strong-motion prediction in a broadband frequency range from a large fault is difficult because the complex nature of the source, path, and site must be represented with the same degree of accuracy.

There are several methods for simulating strong motions as waveforms on a surface at a target site located at an arbitrary position. One is a theoretical method in which wave generation at a source, propagation from the source to a site, and local site amplification near the site are represented by numerical modeling of the medium. In this method, a viable physical model of the medium is required to represent the wave-propagation phenomena in the entire path from the source to the target site. In other words, Green's function must be calculated quantitatively for a point source on the fault surface. Because of the limited computational resources and accuracy of the geophysical model that can be used, the frequency range of such a theoretical method is usually limited to a lower frequency range below 1 Hz, although several attempts have been made to expand the limit to 5 Hz or higher (e.g., Rodgers et al., 2019). Another method is an empirical method in which we use the observed ground motions of a small earthquake or a set of earthquakes as a substitute for Green's function and sum all the contributions from the element sources on the fault surface. This is called the empirical Green's function (EGF) method. The EGF has been proven to be very effective in reproducing the observed mainshocks if we use proper aftershock records (e.g., Kamae and Irikura 1998; Kamae and Kawabe 2004).

Suppose that there are no appropriate small earthquake records to be used as empirical Green's functions, as is the case for ground-motion prediction for future events. In this case, we first generate synthetic waveforms representing small earthquakes and then sum them to represent a large event, as in the EGF. This is called either the stochastic or statistical Green's function method (SGF); the difference between them is explained later. SGF is very useful for predicting strong motions for events that have not yet occurred or that have not yet produced any weak motions.

Because the frequency range for the fully theoretical method with a coherent nature is limited to the lower end, usually below 1 Hz or lower, whereas the valid range for EGF or SGF with the inherent nature of stochasticity is higher, a hybrid scheme combining a theoretical method with EGF or SGF is naturally used. This hybrid method has been used as a standard method in current national projects for strong-motion prediction using specific sources in Japan (J-SHIS 2020).

However, after the deployment of dense national strong-motion observation networks, namely K-NET and KiK-net by the National Institute of Earth Science and Disaster Resilience (NIED), and the Seismic Intensity seismometer (Shindokei) network by the Japan Meteorological Agency (JMA), a significant amount of data has been accumulated, which can be used to construct a model of SGF in a broadband frequency range that can reflect the average characteristics of observed ground

motions. As long as we can generate the SGF for an arbitrary size of a small earthquake at an arbitrary location in the frequency range of interest (in this study, from 0.1 Hz to 20 Hz), we need not use a hybrid scheme combined with a theoretical representation of the low-frequency component for a broadband simulation. The effectiveness of such a broadband use of the statistical Green's function for ground-motion prediction of not-yet-occurring inland earthquakes is shown in Itoh et al. (2001) and Ho and Kawase (2007).

However, if the true complex crustal structure is known, a hybrid scheme can reflect the path- or site-dependent characteristics of wave propagation inside such a structure. In contrast, statistical Green's function modeling can reflect medium- or event-specific characteristics only as statistical deviations from the average. If they are emerging only in a limited area or event, then their effects cannot be seen because their contributions could be too small to alter the average.

For SGF modeling, we used statistical Green's functions based on the generalized spectral inversion technique (GIT, Andrews 1986; Iwata and Irikura 1988) to observe strong-motion data in Japan. The GIT provides the statistical properties of three major terms, namely the source, path, and site terms, as reported by Kawase and Matsuo (2004), Nakano et al. (2015), Nakano et al. (2019), and Nakano and Kawase (2021). The novelty of the approach in these GIT studies is that we use the extracted seismological bedrock spectra at one site, YMGH01, as a reference to calculate the site amplification factors at all other observed sites. We performed GIT for the observed Fourier amplitudes and phase spectra. Such separation of the observed spectra into three major terms in both amplitude and phase is sufficient to generate SGF at these sites using inverse Fourier transforms.

Here, we would like to explain the reason why we call our Green's function as the "statistical" one, rather than the "stochastic" one. The stochastic Green's function, which was initially proposed by Boore (1983) based on a predefined ω^{-2} source spectrum and a specific time window shape, was applied to artificially generated white noise. Since then, many studies have been published using different implementations of the stochastic Green's function. A recent addition to these studies was conducted by Ji et al. (2022). The word "stochastic" means that the Green's function is somehow randomly generated without referring to a specific characteristic derived from the observation. It is acceptable as long as Green's function is used only in the reproduction of the high-frequency range, where the stochastic nature is dominant. In contrast, in the statistical Green's function construction described in this study, we use the Green's function directly obtained from the statistical properties of the observed Fourier amplitude and phase information based on the observed ground motions using the generalized inversion technique (GIT). The merit of using the statistical Green's function is its reality as a substitute for the empirical Green's function in the broadband frequency range because of the direct connection of the characteristics to the observed small earthquakes of the same size as the element source used for summation. Another merit is the option to consider the effects of variations in the source, path, and site factors derived directly from the statistics of the observed ground motions, if we want to consider such variations. Before this implementation, the statistical Green's function method was applied to the subduction plate-boundary earthquakes by Baoyintu et al. (2013, 2021), where they only used amplitude information from GIT. Instead, they used an envelope function with coefficients obtained by the regression for magnitude and distance.

After constructing the Green's function, which can be used under generic conditions, the next step comprises a complex source representation of the fault for realistic synthetics of broadband ground motions.

From the beginning of kinematic source modeling in strong-motion seismology in the late'70 s and the early'80 s, it is apparent that we need to introduce spatial heterogeneity into slip distributions (Das and Aki 1977; Aki 1979; Papageorgiou and Aki, 1983 for Barrier model and Lay and Kanamori 1981 for Asperity model). In the'80 s and'90 s source process, inversion studies were conducted on major earthquakes worldwide. We can now refer to the SRCMOD database collected by Mai and his group (http://equake-rc.info/srcmod/) to see those events analyzed before 2000.

For inland crustal earthquakes, Mai and Beroza (2002) referred to the kinematic source inversion results of 44 previous seismic events collected at that time to obtain a stochastically randomized source model with a fractal structure by considering the correlation distance with respect to the corner wave number, kc. Guatteri et al. (2003) performed a strong ground-motion simulation from rupture scenarios constructed based on the stochastic source model of Mai and Beroza (2002) and showed its validity by comparing the simulated results with empirical predictions using the ground-motion prediction equation (GMPE). Graves and Pitarka (2004, 2010, 2016) performed strong-ground-motion simulations of the past four earthquakes in the U.S. and validated the resultant strong ground motions by comparing them with the observed the peak ground accelerations (PGAs), the peak ground velocities (PGVs), and acceleration response spectra.

However, a stochastically randomized source model with small-scale variations cannot reproduce

large-amplitude velocity pulses owing to the forward rupture directivity from a distinctive patch or asperity (i.e., asperity pulses), which is characteristic of strong ground motions in the near-fault region directly connected to structural damage in the epicentral regions of crustal earthquakes (Kamae and Irikura 1995; Pitarka and Irikura 1996; Kawase et al. 2000). Because it was found that the waveform of the near-fault region of the 1995 Hyogoken Nanbu earthquake was primarily composed of these asperity pulses (Kamae and Irikura 1995; Kawase et al. 2000), a method for extracting several large slip areas of the source and modeling them according to the scaling law of the outer fault parameters (e.g., Somerville et al. 1999) has been developed in Japan. The resulting source model is called the characterized source model (Irikura and Miyake 2001; Irikura et al. 2004).

The validity of the strong ground motions reproduced based on this characterized source model was demonstrated by comparing the observed records of several past earthquakes (Miyakoshi et al. 2000; Miyake et al. 2003; Miyakoshi et al. 2004). To systematize the method, Irikura and Miyake (2001) proposed a procedure (the so-called "recipe" for strong-motion prediction) to construct a characterized source model with distinct strong-motion-generation areas (SMGAs) by analyzing observed records of several past earthquakes. However, such a distinctive SMGA representation for source complexity is problematic because the theoretical Green's function emphasizes only the wave motions from the SMGAs. Therefore, the reality of the envelope form over the entire observed duration would not be well reproduced.

As part of the activities in the broadband strong-motion prediction platform project within the Southern California Earthquake Center (SCEC), Pitarka et al. (2020) validated the stochastically randomized model by Graves and Pitarka (2016), characterized source model by Irikura and Miyake (2011), and a hybrid model that combines the two models by comparing the synthetic strong ground motions from those models with those observed during the 2016 Kumamoto earthquake, as well as the model bias with respect to GMPEs. As a result, both the hybrid model and each of the two models show that they can generally reproduce the acceleration response spectra of the observations equally well.

However, when we look at subduction-zone earthquakes macroscopic source rupture processes have also been studied since the early'80 s using recorded long-period seismic waveforms from distant locations (e.g., Kanamori 1981; Lay and Kanamori 1980, 1981; Kikuchi and Kanamori 1982, 1986, 1991). Long-period source inversions have revealed that the slip distribution on a fault plane is heterogeneous, as observed in crustal earthquakes. The large slip areas (asperities) determined in these studies exhibited slight variations, reflecting the resolution limit of the seismic waves used.

Irikura et al. (2004) and Miyake et al. (2006) proposed a method (recipe) for constructing a source model that can reproduce up to short periods based on the results of an analysis of past subduction-zone earthquakes as well as inland crustal earthquakes, and strong-motion predictions have been made using this method (e.g., Kamae and Kawabe, 2004). However, the number of subduction-zone earthquakes that have occurred in the past around Japan is much smaller than that of crustal earthquakes. Consequently, it is not easy to sufficiently verify the recipe.

Sekiguchi and Yoshimi (2011) proposed a method for constructing a heterogeneous source model based on the method of Mai and Beroza (2002) to add stochastic randomness to the distinct SMGAs proposed by the Central Disaster Prevention Council (2003). The basic concept of the stochastic slip distribution is similar to that of the hybrid model of Pitarka et al. (2020). Based on these reports on the complex nature of the fault rupture process, it is important to introduce both a coherent nature for asperities or SMGAs and a stochastic nature for the entire fault surface to represent realistic features observed in the simulated waveforms. In this regard, we are not trying to improve the implementation of complex source modeling in the scheme of Sekiguchi and Yoshimi (2011). Rather, we are trying to observe the effects of complex source modeling on the simulated waveforms in terms of spectra and maximum amplitudes when we combine it with the statistical Green's functions mentioned above.

Then, the M 9.0 off the Pacific coast of Tohoku Earthquake occurred on March 11, 2011. The results of source inversion of the earthquake showed that a large slip region related to tsunami generation was located near the trench axis. In contrast, strong-motion generation areas (SMGAs) with a period of down to 2 s, which are directly related to the cause of building damage, are located on the western side of the ruptured area (e.g., Lay et al. 2012; Asano and Iwata, 2012; Kurahashi and Irikura, 2013). This finding is consistent with the depth dependence of the Brune's stress parameter (the deeper, the larger) reported by Nakano et al. (2015).

Basic strategy

To construct a more realistic source model, it is necessary to construct a heterogeneous source model based on knowledge obtained from the latest megathrust earthquake. Therefore, in this study, we constructed a heterogeneous source model by arranging the size and locations of SMGAs based on the recipe and findings from the 2011 Tohoku earthquake, together with random perturbations in both the SMGAs and background regions

using the method of Sekiguchi and Yoshimi (2011). As will be mentioned later, we introduce a partially stochastic nature to the phase characteristics of all statistical Green's functions. Therefore, it is interesting to observe the effects of heterogeneity introduced in the rupture process of the hypothesized source under this partly stochastic SGF representation.

In this study, as a primary step toward understanding the source rupture process of the 1944 Tonankai earthquake, we combined the statistical Green's function proposed by Nakano and Kawase (2021) and the heterogeneous source model proposed by Sekiguchi and Yoshimi (2011) to reproduce the strong motion of an earthquake. It is worthy of note that the 1944 Tonankai earthquake was an M8 class subduction plate-boundary earthquake (e.g., Ando 1975) whose entire source has not been understood in detail because of the lack of observed waveforms in the near-fault region. The validity of the heterogeneous source model and the effects of introducing heterogeneity will be confirmed. The remainder of this paper is organized as follows. First, we briefly explain the GIT approach proposed by Nakano and Kawase (2021) and the resultant separate site amplification factors necessary for calculating Green's function. Then we show the proposed concept of basin-induced surface waves and coda waves that can be represented by the whole-wave to S-wave spectral ratio (WSR). We also demonstrate how to represent the group delay time, as proposed by Nakano and Kawase (2021). The amplitude and phase spectra of an incident wave at an arbitrary site from an element source on a fault surface are necessary to calculate the synthetic Green's function. We then explain the method of constructing the heterogeneous source model from the SMGA distribution, based on the model of the Cabinet Office (2015) and the method of Sekiguchi and Yoshimi (2011). Based on this method, we constructed models with (i) various slip values and a constant rupture velocity (CASE-VScr); (ii) a constant slip value and a constant rupture velocity (CASE-CScr); and (iii) both various slip and rupture velocity values (CASE-VSvr). To compare the validity of these models and the Green's functions used, we show the PGA and PGV distributions as a function of the distance and spectral amplitudes of selected sites for each case, together with a couple of representative acceleration time histories. The effects of heterogeneity on the PGA and PGV were studied by comparing Case-VScr with Case-CScr and Case-VScr with Case-VSvr. In addition, the effect of nonlinearity in the resultant synthetics, based on the approximated method proposed by Nakano and Kawase (2021), was investigated as Case-VScrNL. Through these analyses, we demonstrate that the proposed method is reasonable for predicting strong ground motions from a megathrust event. Please note that we previously published part of this study in the DPRI Annuals, the institutional collection of research reports from DPRI researchers (Ito et al. 2020a).

Statistical green's function

Outline of GIT

In this section, we briefly introduce the observed horizontal site amplification factor (HSAF) and vertical one (VSAF) derived from GIT (Nakano et al. 2015; Nakano and Kawase 2021). Here, we only introduce their basic aspects because we used their results as a starting point.

Based on the ordinary nonparametric GIT concept, the S-wave Fourier spectrum of the horizontal motion, F_{S_ij}, of earthquake i observed at site j is decomposed into the common logarithmic sum of the source term S_{S_i}, path term P_{S_ij}, and the horizontal site amplification factor at site j, H_{S_j}, as shown in the following equations:

$$\log F_{S\_ij} = \log S_{S\_i} + \log P_{S\_ij} + \log H_{S\_j} \tag{1}$$

Similarly, the S-wave Fourier spectra of the vertical motion G_{S_ij} is decomposed into the following equation:

$$\log G_{S\_ij} = \log S_{S\_i} + \log P_{S\_ij} + \log V_B H_B R + \log V_{S\_j} \tag{2}$$

From these equations, the separation of variables through the GIT analysis should be performed simultaneously for both the horizontal and vertical components to obtain the common source and path terms. Otherwise, we may have slightly different source and path terms for the horizontal and vertical components.

These equations assume that ground motion from the source is propagated as S-waves until it reaches the seismological bedrock immediately below the observation site, after which a part of the energy of the S-waves is converted to P-waves, which are observed as a vertical motion on the ground surface after amplification through the layers above the seismological bedrock. Here, V_{S_j} is the vertical site amplification factor for site j, and the third term on the right-hand side of Eq. (2), $V_B H_B R$, is a coefficient accounting for the ratio of the vertical amplitude of an S-wave part V_B to the horizontal amplitude of the same S-wave part H_B under the equipartition condition of DFC. This term corresponds to the inverse of the horizontal-to-vertical amplitude ratio of the incident wave at the seismological bedrock, which is theoretically equal to the square root of the ratio of the P-wave velocity to the S-wave velocity of the seismological bedrock in the diffuse field regime (e.g., Kawase et al. 2011; Nagashima et al. 2014; Ito et al., 2020b). Therefore, this coefficient should be virtually frequency-independent. However, we observed some small fluctuations around the theoretical value at the reference site, YMGH01, as

shown in Ito et al. (2020b). This coefficient is required because the main portion of the wave energy consists of S-waves propagated and scattered through the medium from the hypocenter to the point on the seismological bedrock immediately below the site, whereas V_{S_j} represents the vertical (P-wave) amplification factor of the vertical component from the seismological bedrock to the surface. HSAF and VSAF are the general terms referring to the site amplifications in the horizontal and vertical directions, while H_{S_j} and V_{S_j} are the specific terms derived from GIT at site *j*. Therefore, we refer to the horizontal and vertical site amplification factors as HSAF and VSAF hereafter for simplicity.

We restricted events and sites with JMA magnitude $M_{JMA} \geq 4.5$; source depth ≤ 60 km; hypocentral distance ≤ 200 km; peak ground acceleration ≤ 2 m/s^2; and number of observation sites triggered simultaneously for one event ≥ 3. These selection criteria resulted in 77,213 event-station pairs at 2,105 sites for 967 events from the K-NET, KiK-net, and JMA Shindokei networks. Only a relatively short duration of acceleration record from the onset of the S-wave is analyzed (5 s if $4.5 < M_{JMA} \leq 6$; 10 s if $6 < M_{JMA} \leq 7$; 15 s if $7 < M_{JMA} \leq 8$) to focus on the S-wave part. The contributions of basin-induced and basin-transduced surface waves as well as coda waves were evaluated separately, as explained in the next section. A Parzen window of 0.1 Hz was used as the minimum level of smoothing. As mentioned above, the most important feature of the GIT used here is that it determines the S-wave velocity structure at the reference site (YMGH01) using the transfer function (the spectral ratio and the phase difference) between the surface and the borehole 200 m below, and deconvolves the observed Fourier spectra on the surface to obtain the hypothesized outcrop spectra on the seismological bedrock with an S-wave velocity of 3,450 m/s. Nakano et al. (2015), Nakano et al. (2019), and Nakano and Kawase (2021) successfully separated the source spectra and path terms as evidenced by their correspondence to the ω^{-2} source spectra shapes and regional Q values (transformed from the path terms) similar to previous studies in Japan.

Here, we emphasize the importance of the reference spectral conditions used in the GIT. It is acceptable to use any site or sites with any site amplification factors as a reference site or sites. However, if we use a site with site amplification as a reference, all the site amplifications will be carried over to the source factors for all events used. This is a direct consequence of Eqs. (1) and (2): If we set one site as a reference site, it is equivalent to assume that H_{S_j} at the reference site is one (i.e., log H_{S_j} is zero); therefore, the actual amplification at that site, if it exists, should be included in the source spectrum S_{S_i}. This is because the path term is strongly constrained by all paths between the source-to-site pairs. However, the source and site terms are interconnected simply as a sum in the logarithmic space. If several sites are selected as a group of reference sites, their average amplification factor is carried over to the source spectrum. This situation is true not only for GITs, but also for any GMPEs. Therefore, the modeled source spectra in any GMPEs with a reference site condition not specifically defined as the outcrop of the seismological bedrock with a sufficiently high surface S-wave velocity (Vs≧3 km) would be higher than the true source spectra by the amount of the actual site amplification included in the reference spectra.

Figure 1 shows examples of separated HSAF and VSAF at four representative sites in the Mie Prefecture, directly derived from Eqs. (1) and (2) as H_{S_j} and $V_B H_B R^* V_{S\_j}$. The choice of these sites was somewhat arbitrary; they were selected from a region relatively close to the epicenter. Among them, three were from the hilly zones of the Shima District with relatively stiff soil layers, and the other (JMAE43) was located close to the edge of the Ise Basin. We observed significant differences in HSAF from site to site. The amplitude and fluctuation of the VSAF were much smaller than those of the HSAF, especially below 3–7 Hz. Therefore, the earthquake horizontal-to-vertical spectral ratio, eHVSR, tends to be like HSAF until the fundamental peak frequency of VSAF is reached. However, to obtain HSAF from eHVSR, we need to correct VSAF, as recently proposed by Ito et al. (2020b). The VSAFs shown in Fig. 1 are the site amplification factors of the vertical component with respect to the horizontal component of the seismological bedrock, referred to as VSAF* by Ito et al. (2020b). VSAF* corresponds to VSAF multiplied by $V_B H_B R$; thus, VSAF* is slightly (theoretically 72%) smaller than VSAF. Hereafter, we use the abbreviation "VSAF" simply to refer to $V_B H_B R^*$VSAF without any confusion, because we specifically predict the S-wave part of the spectra radiated from the source. Therefore, we need to use the relative amplification factor of the vertical component to the S-wave input on the seismological bedrock (H_B). Please note that we have not yet included a P-wave portion in our ground-motion simulations.

WSR to account for basin effects

One of the novelties of our SGF based on the GIT is the back calculation of the site factors for the entire duration of motion. When our target sites are located within a sedimentary basin, we observe additional amplification due to basin-induced or basin-transduced surface waves generated at the edge of a 2D or 3D basin (e.g., Bard and Bouchon 1980; Kawase and Aki 1989; Kawase 2003), in addition to the contribution of the S-wave coda. They were significant in the lower frequency range (< 1 Hz),

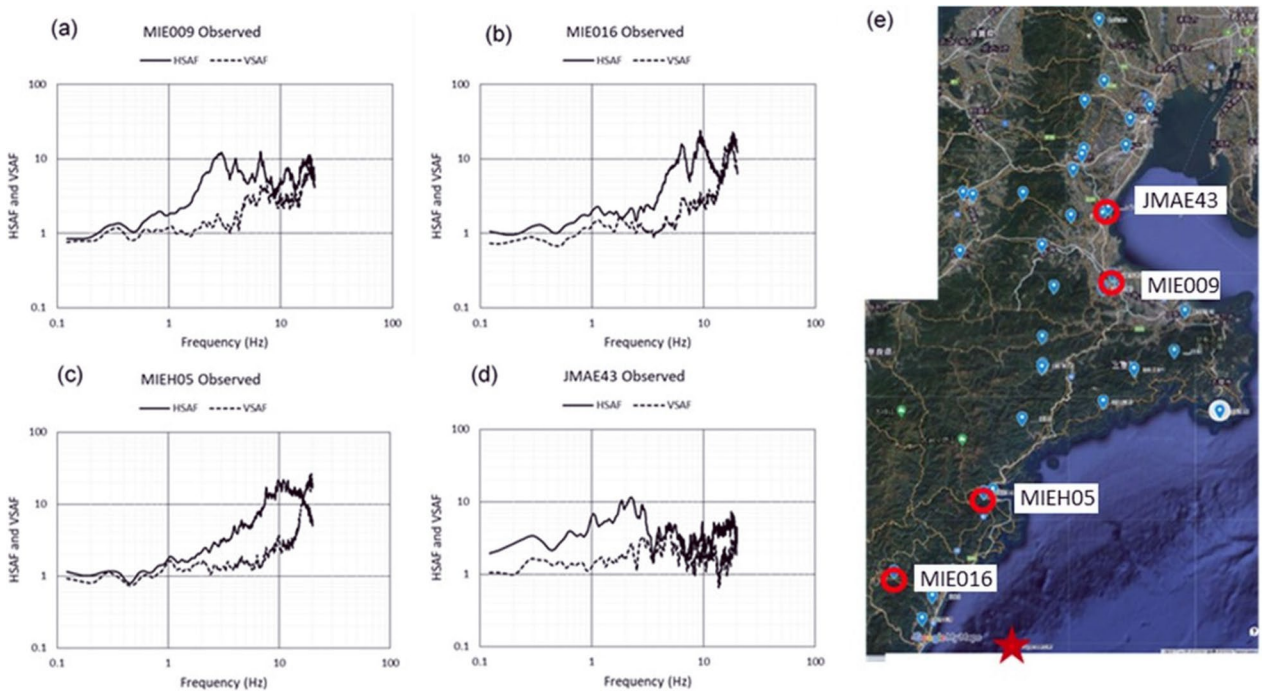

Fig. 1 Site amplification factors (HSAF and VSAF) at four sites in the Mie Prefecture **a**–**d**; the locations are shown in the map (**e**). They were extracted from the S-wave part of the records in K-NET, KiK-net, and JMA Shindokei networks (Nakano et al. 2015). A rupture initiation point (★) is also indicated in the map (**e**)

especially inside soft and large basins. However, if we directly used the entire duration of motion as the target of GIT analysis, the resultant attenuation would be distorted. When we use the entire duration, the Fourier spectra inside a basin but away from the source become larger than those spectra at sites closer to the source but outside of a basin. As a result, we cannot observe any attenuation in proportion to the distance; hence, we will have negative Q values.

To account for the effects of basin-induced and basin-transduced surface waves inside sedimentary basins, Nakano and Kawase (2019) and Nakano and Kawase (2021) proposed the use of an empirical ratio called the whole-wave-to-S-wave ratio (WSR), where the spectral ratios of the whole duration with respect to the S-wave portion with a relatively short duration (5–15 s) are averaged over all the observed events at a site. Although we have never performed another GIT for the entire duration, conceptually, we are doing the same as the GIT analysis for the whole-wave Fourier spectra of the horizontal motion, F_{W_ij}, based on the following equation:

$$\log F_{W\_ij} = \log S_{S\_i} + \log P_{S\_ij} + \log H_{W\_j} \tag{3}$$

where H_{W_j} is the whole-wave horizontal site amplification factor at site j. We fixed the source and path terms as those obtained for the S-wave part. Similarly, the whole-wave Fourier spectra of the vertical motion G_{W_ij} were decomposed into the following equation:

$$\log G_{W\_ij} = \log S_{S\_i} + \log P_{S\_ij} + \log V_B H_B R + \log V_{W\_j} \tag{4}$$

where V_{W_j} is the whole-wave vertical site amplification factor at site j. WSR is the ratio of either H_{W_j}/H_{S_j} or V_{W_j}/V_{S_j}. Surprisingly, we found that the WSR for the horizontal and vertical components were quite similar. Therefore, we applied the same WSR for both the horizontal and vertical components after spatial interpolation, as described below.

We found that the WSR tends to be close to 1 irrespective of the frequency of a site on hard rock, whereas it can easily exceed 10 in the lower frequency range for a site inside a soft sedimentary basin. Even for such a site, the WSR converges to 1 (or close to 1) toward a higher frequency range, usually higher than 1 or 2 Hz. In Fig. 2, the averaged HSAFs for only the S-wave part (black line) and those for the whole duration (red line) with their variation (red dotted lines) are compared. Thin gray lines represent individual HSAFs for the whole duration. MIE009, MIE016, and MIEH16 show the normal characteristics of sites outside a sedimentary basin, whereas JMAE43 shows those inside a deep (> 1 km) sedimentary basin close to the shoreline.

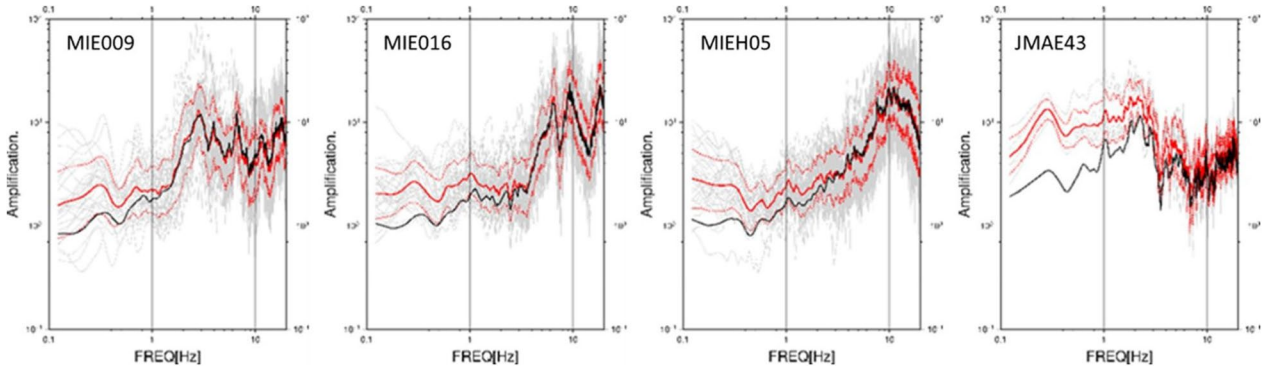

Fig. 2 HSAFs for the S-wave portion in Fig. 1 (black) and those for the whole duration (red). The black line is the average of the S-wave portion, while the red line and red dotted lines are the average and average ± one standard deviation for the whole duration, respectively. Thin grey lines are individual HSAFs for the whole duration

The WSR is the spectral ratio between the red and black lines in this figure.

The spatial variation of WSR at a specific frequency is highly correlated with that of the basin depths, as reported by Nakano and Kawase (2019). Nakano and Kawase (2021) proposed a scheme to interpolate WSRs to make it possible to calculate a scenario-type hazard map with a much higher spatial density (in a 250 m grid) than those of strong-motion observation sites. The interpolation scheme utilizes the surface function of the GMT (Smith and Wessel 1990), together with the code developed by Renka (1999). This WSR correction is a simple empirical method that accounts for additional amplifications caused by soft sedimentary basins. In Fig. 3, we plot the original WSRs for HSAF across Japan and those interpolated based on the scheme proposed by Nakano and

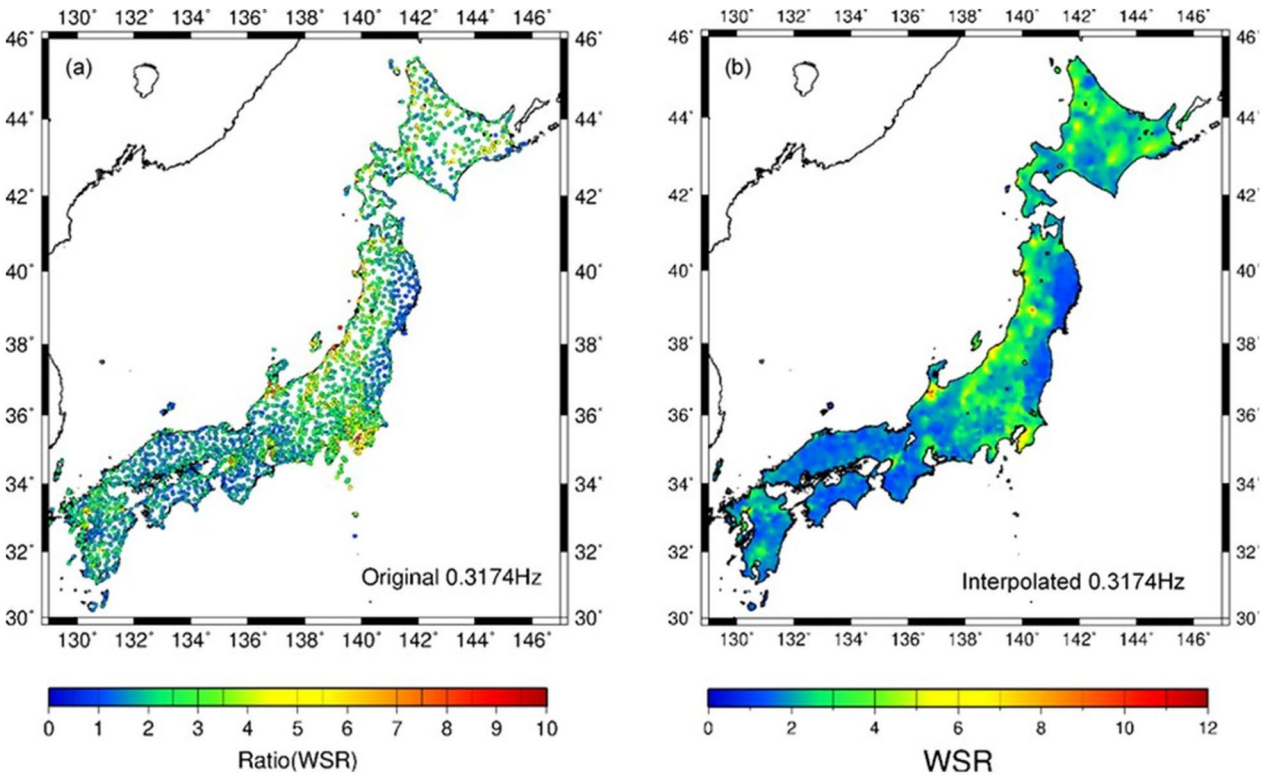

Fig. 3 Comparison of the two WSRs obtained in two different ways. WSRs calculated from the observed data are plotted in (**a**), and those interpolated to higher spatial resolution through the proposed interpolation scheme are plotted in (**b**)

Kawase (2021) at 0.3174 Hz. It is evident that the WSR corrections are significant in the lower-frequency range inside the large sedimentary basins, especially in Eastern Japan, east of the Itoigawa–Shizuoka tectonic line.

Tgr modeling

To calculate the broadband synthetic waveforms for small-to moderate-sized earthquakes as SGFs, we must specify their phase information or envelope functions to constrain the time-varying characteristics of the synthetic SGFs as a function of frequency. It is desirable to use phase spectral information because it can account for the frequency dependence of the envelope shape (Sato et al 2002; Satoh 2004). Thus, we followed the procedure of Nakano and Kawase (2021) to model the group delay time t_{gr} as

$$t_{gr} = \frac{d\varnothing(\omega)}{d\omega}, \tag{5}$$

where,

$$\emptyset(\omega) = \tan^{-1}\left(I(\omega)/R(\omega)\right), \tag{6}$$

From Eqs. (5) and (6), following Satoh (2004), we use the following equation:

$$t_{gr} = \frac{R(\omega)\cdot I(\omega)^{'} - R(\omega)^{'}\cdot I(\omega)}{R^2(\omega) + I^2(\omega)} \tag{7}$$

where $R(\omega)$ and $I(\omega)$ are the real and imaginary part of the spectra and $func(\omega)^{'}$ means the differentiation of $func(\omega)$ with respect to ω. Then, we can model the average and variance characteristics of t_{gr} for the whole duration of observed record $\mu(f)$ and $\sigma(f)$ as

$$\mu\_ij(f) = \mu^{Source\_i}(f) + \sum_k \mu_{ijk}^{pass}(f)\cdot X_{ijk}^{1.9} + \sigma^{Site\_j}(f) \tag{8}$$

$$\sigma\_ij(f) = \sigma^{Source\_i}(f) + \sum_k \sigma_{ijk}^{pass}(f)\cdot X_{ijk}^{1.9} + \sigma^{Site\_j}(f) \tag{9}$$

for the i-th source observed at the j-th site. The derivation of these equations is the same as that of the GIT for spectral amplitudes, that is, Eqs. (1) and (2), except for the fixed geometrical spreading factor of 1.9, based on a study by Satoh (2004). X_{ijk} is the apparent section of the entire path in the k-th region (k = 1, 6). Please refer to Nakano et al. (2015) for information on separate regions of path effects. The reference site for t_{gr} was also YMGH01, and t_{gr} at that site was set to zero. In the actual SGF calculation, we introduced a random number for each frequency to consider $\sigma(f)$ as the perturbation from the average t_{gr}, $\mu(f)$.

In Fig. 4, we showed examples of the site terms in Eq. (8), that is, $\mu^{Site\_j}(f)$, for the same sites shown in Figs. 1 and 2. The physical meaning of the average site terms, $\mu^{Site\_j}(f)$ is the difference of the peak-out time relative to that at YMGH01. Although we omitted any examples here, the physical meaning of the variance, $\sigma^{Site\_j}(f)$ is the spreading characteristics in time (i.e., the width of the main duration). Among the four sites, only JMAE43 site shows a significantly longer duration, especially in the lower-frequency range, owing to the basin-induced surface waves of the Ise Basin. As for the vertical component, we used the same $\mu^{Site\_j}(f)$ and $\sigma^{Site\_j}(f)$ as the horizontal component based on the comparison of t_{gr} for the horizontal and vertical components.

Stochastic source model

A broadband heterogeneous source model was generated for a plate boundary earthquake along the Nankai Trough by introducing fractal heterogeneity into a characterized source model consisting of background and strong-motion generation regions.

The gross ruptured area (i.e., the assumed fault plane) of the fault map of the Central Disaster Management Council (CDMC, 2003) was projected onto the upper surface of the Philippine Sea plate of the Japan Integrated Velocity Structure Model (JIVSM; Koketsu et al. 2012) and adjusted to be compatible with the fault size of the CDMC, and included the strong-motion generation areas (SMGAs) of the Cabinet Office (2015). For the assumed SMGAs, their areas, moments, stress parameters, rise times, and center positions were adopted from the values provided by the Cabinet Office (2015) as the basic model (Table 1). However, the shape

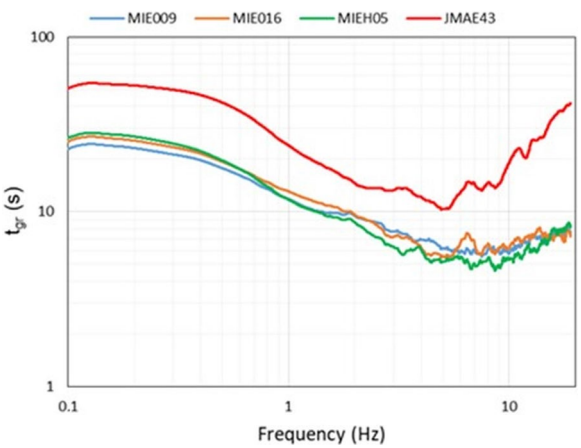

Fig. 4 Site factors for the average t_{gr} extracted by GIT shown as Eq. (8) for the whole duration of records. These t_{gr} are used as a part of the phase information needed to calculate element Green's functions for ground-motion simulation

Table 1 Fault parameters for the 1944 Tonankai earthquake (After CDMC, 2003)

Region	Area [km^2]	Moment [Nm]	Mw	Average slip [m]	Stress parameter [MPa]	Rise time [s]	Center location		
							Latitude	Longitude	Depth[km]
Entire fault	15,944	2.63e21	8.2	3.68	n/a	n/a	33.70[a]	136.25[a]	13[a]
SMGA 1	714.2	2.18e20	7.5	6.77	30.0	4.9	34.70	135.75	16
SMGA 2	913.5	3.13e20	7.6	7.64	30.0	5.6	34.60	137.10	24
SMGA 3	613.6	2.00e20	7.5	7.26	30.0	4.6	34.00	136.60	18
SMGA 4	615.8	1.81e20	7.4	6.59	30.0	4.6	33.70	136.25	13
Background	13,087	1.71e21	n/a	2.91	2.4	10.0	n/a	n/a	n/a

[a] Location information here is the rupture starting point

of the SMGA is assumed to be circular, unlike those of the Cabinet Office (2015). We assumed as such because we want to use an automatic generation system for a large number of parametric studies with various locations and areas of SMGAs in the future. We also believe that circular and half-circular shapes may work as representative shapes for SMGAs based on the spatial distribution of large-slip areas from past kinematic source-process inversions. The parameters of the background region of the basic model were based on CDMC (2003). The amount of average slip was calculated from the total moment and fault area, similar to the method used by the CDMC (2003). The average area of each fault element was approximately 25 km^2, with some variations. The averaged seismic moment of each element is 4.3×10^{18} N·m.

Broadband source heterogeneity was calculated by randomly adding the heterogeneity of slip distributions from approximately half of the SMGA areas to several km^2 in size to the basic source parameter distribution consisting of the background and SMGAs, as described by Sekiguchi and Yoshimi (2011). The amplitude of the fluctuation was proportional to the size of heterogeneity. The power of the fall-off in the spatial distribution of the slip heterogeneity was adjusted and is equal to the value obtained by Mai and Beroza (2002), i.e., − 1.75. The stress parameter distribution is proportional to the variation in the slip distribution. In the end, the level of introduced slip heterogeneity in terms of the standard deviation was turned out to be approximately 1.3 m for the entire fault area.

The rupture velocity distribution was started from a uniform distribution of 2.7 km/s and a constant amount of variation regardless of the area of the inhomogeneous patch was added and finally adjusted so that the standard deviation of the spatial variation was set to ± 20% (Sekiguchi and Yoshimi 2011). This is equivalent to the level obtained by Miyakoshi and Petukhin (2005) in their analysis from the source-inversion models. We set the maximum allowable rupture velocity to be the S-wave velocity of the seismogenic zone. The distribution of rupture arrival times at an arbitrary point on the fault was obtained through wave-propagation analysis using an ordinary two-dimensional finite difference method with a perturbed (or constant) rupture velocity on the fault surface.

Figure 5 shows the assumed shape of the whole ruptured area and the SMGAs, together with the locations and names of the prefectures that were damaged by the 1944 Tonankai earthquake. Randomized slip and randomized rupture velocity on the stochastic fault model used for strong-motion simulations are shown in Fig. 6 and 7, respectively, and the results are shown in the next section.

Results of parametric studies

In this chapter, to observe the effect of the variable slip and rupture velocity proposed by Sekiguchi and Yoshimi (2011), we tested three scenarios: a model with variable slip values and a constant rupture velocity (CASE-VScr), a model with a constant slip value and

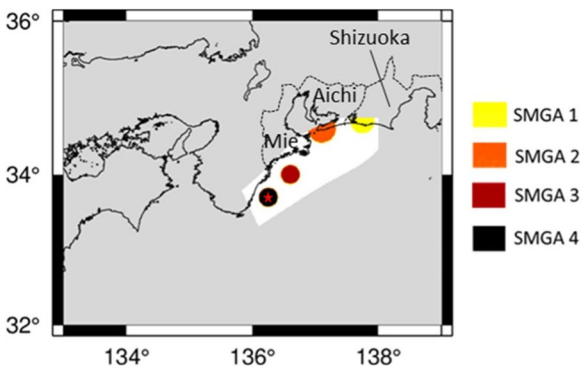

Fig. 5 Predefined SMGAs and the whole fault area for simulating the 1944 Tonankai earthquake. The name of each prefecture (i.e., Mie, Aichi, and Shizuoka) is also shown in the figure. A rupture initiation point is indicated by a star (★)

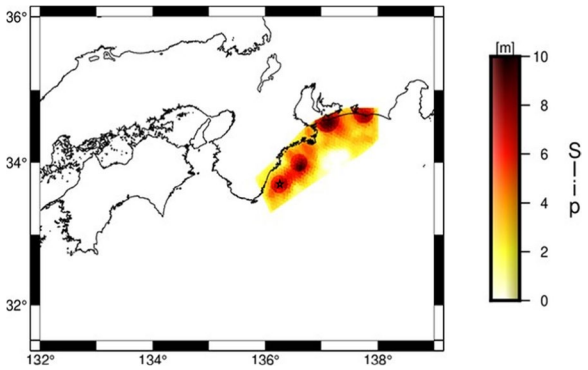

Fig. 6 Randomized slip distribution on the stochastic fault model of the 1944 Tonankai earthquake. A rupture initiation point is indicated by a star (★)

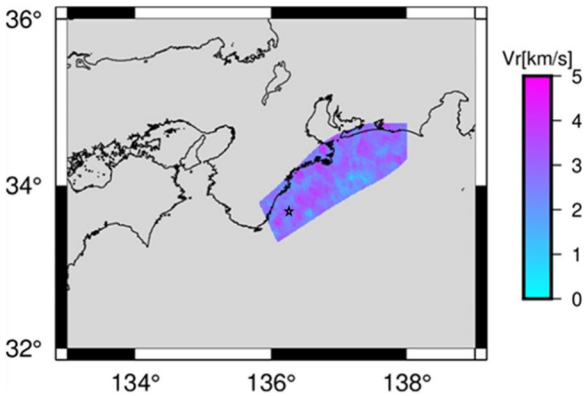

Fig. 7 Randomized rupture velocity on the stochastic fault model of the 1944 Tonankai earthquake. A rupture initiation point is indicated by a star (★)

a constant rupture velocity (CASE-CScr), and a model with variable slip values and rupture velocities (CASE-VSvr). We calculated the PGAs and PGVs at the K-NET, KiK-net, and JMA Shindokei networks in the Mie, Aichi, and Shizuoka Prefectures, where severe building damage and tsunamis were observed during the 1944 Tonankai earthquake (Takemura and Toraya, 2015). All target sites used in this study are listed in Table 2 with their altitudes. Table 2 also includes Vs30 (the so-called time-averaged S-wave velocity of top 30 m) from the PS logging data as in Wang et al. (2023) for K-NET and KiK-net sites or from the estimated shallow velocity profiles of Senna et al. (2019) and Wakai et al. (2019) for JMA sites, as well as Z1.4 (the depth to the layer with the S-wave velocity higher than 1.4 km/s) from the estimated deep velocity profiles of Senna et al. (2019) and Wakai et al. (2019). These are the site parameters in the empirical formula of Morikawa and Fujiwara (2013).

Model with variable slip and constant rupture velocity (CASE-VScr)

Figure 8 shows the attenuation relationships of the PGA and PGV in CASE-VScr with respect to the shortest distance to the fault plane. The orange and blue circles show the PGA and PGV at each site, respectively, the black line shows the empirical relationship from Model 2 of Morikawa and Fujiwara (2013), and the black dotted lines show the average plus/minus one standard deviation. CASE-VScr yields strong-motion synthetics with PGAs that correspond to slightly higher values than the empirical relationship of Morikawa and Fujiwara (2013), whereas PGVs tend to correspond to the average values. We used the baseline attenuation formulas in Morikawa and Fujiwara (2013), where Vs30 is assumed to be 350 m/s and Z1.4 to be 0.1 km. These reference values would be appropriate for sites outside large basins, such as MIE016. However, these references would be too large for Vs30 and too small for Z1.4, for sites inside large basins, such as JMAE43. If we consider the range of effects in these site parameters for typical values inside large basins, such as Vs30 = 200 m/s or Z1.4 = 1 km, the deviation from the baseline shown here would yield a 1.3 to 1.5 times increase (See Morikawa and Fujiwara (2013) for detailed information). To see the effects of Vs30 and Z1.4 in the simulated PGA and PGV, we distinguished the basin sites with Vs30 < 250 m/s and Z1.4 > 500 m (14 in total) with small solid circles inside. In Fig. 8, as well as the other figures with different source parameters, namely, Figs. 13 and 15, we can see clearly the effects of soft and deep sedimentary basins as increasing amplitudes on both PGA and PGV. Relative amplifications are slightly larger in PGV than those in PGA, which is consistent with their difference in coefficients shown in Morikawa and Fujiwara (2013).

Figures 9 and 10 show the acceleration waveforms and the acceleration Fourier and pseudo-velocity response spectra at JMAE43, and Figs. 11 and 12 show those at MIE016 in the same manner. At JMAE43, located inside the Ise Plain, the peaks of the response spectra exist in the period range of 0.5–2 s. At MIE016, which is located inside a hilly zone, the response spectra were much smaller than those at JMAE43, except for the period shorter than 0.3 s. Please note that the east–west (EW) component in the low frequency range is larger than the north–south (NS) component because of the frequency-dependent radiation pattern.

Model with constant slip and constant rupture velocity (CASE-CScr)

Figure 13 shows the attenuation relationships of the PGAs and PGVs in CASE-CScr. The orange and blue

Table 2 List of the target sites used for simulation

Site name	Latitude	Longitude	Altitude[m]	Vs30[m/s]	Z1.4[m]
MIE001	35.1718	136.4943	128	579	639
MIE002	35.0279	136.5073	79	345	1246
MIE003	34.9704	136.6357	2	**238**	**1434**
MIE004	34.8569	136.4493	79	442	794
MIE005	34.7677	136.1151	134	554	96
MIE006	34.7178	136.5039	3	**249**	**997**
MIE007	34.6435	136.3365	52	338	96
MIE008	34.6285	136.1073	221	351	38
MIE009	34.5752	136.5296	32	293	99
MIE010	34.4908	136.7334	19	259	35
MIE011	34.4283	136.3329	143	670	50
MIE012	34.2544	136.8232	8	776	285
MIE013	34.2777	136.4996	2	238	150
MIE014	34.0638	136.1687	85	1238	38
MIE015	33.8783	136.0822	6	546	417
MIE016	33.8764	135.9188	63	485	84
MIE017	34.3624	136.3348	118	573	50
MIE018	34.8702	136.4546	183	457	870
MIEH01	34.9849	136.4563	290	342	475
MIEH02	34.7662	136.2835	280	423	50
MIEH03	34.547	136.3692	280	435	11
MIEH04	34.3532	136.5866	90	490	49
MIEH05	34.0637	136.1689	85	590	96
MIEH06	34.358	136.3293	129	939	40
MIEH07	34.2544	136.8216	10	617	279
MIEH08	34.5424	136.5033	35	1010	43
MIEH09	33.7644	135.9969	90	608	105
MIEH10	34.8224	136.4245	75	422	746
JMABD8	33.8181	136.0255	115	494	37
JMAE4F	34.07	136.1938	101	309	34
JMACD4	34.238	136.2738	74	339	62
JMA929	34.2583	136.8154	10	296	262
JMACD3	34.395	136.7035	167	826	10
JMA549	34.5483	136.5518	14	318	75
JMAD1B	34.7133	136.4168	39	240	382
JMAE43	34.7347	136.5201	3	**192**	**1110**
Site name	**Latitude**	**Longitude**	**Altitude[m]**	**Vs30[m/s]**	**Z1.4[m]**
JMATSU	34.733	136.5201	3	**192**	**1110**
JMAE41	34.7616	136.1419	158	248	139
JMA548	34.8783	136.5685	11	313	1235
JMAE64	34.9399	136.5804	50	350	1210
AIC001	35.2976	136.7499	6	**167**	**720**
AIC002	35.2979	136.9153	20	431	143
AIC003	35.1732	136.7404	− 2	**149**	**1229**
AIC004	35.0632	136.9737	27	332	759
AIC005	35.1979	137.2056	150	496	49
AIC006	35.2159	137.5086	510	327	50
AIC007	35.1394	137.3353	158	342	40
AIC008	35.0977	137.5697	479	635	40

Table 2 (continued)

Site name	Latitude	Longitude	Altitude[m]	Vs30[m/s]	Z1.4[m]
AIC009	35.0812	137.1464	60	300	231
AIC010	34.976	137.4236	538	196	29
AIC011	34.9965	136.8639	5	**229**	**923**
AIC012	34.9119	137.0447	6	211	390
AIC013	34.9335	137.5761	80	635	36
AIC014	34.8263	137.22	4	372	36
AIC015	34.7549	137.4047	8	382	206
AIC016	34.7788	136.9087	6	215	143
AIC017	34.6728	137.2606	10	372	170
AIC018	34.6221	137.1078	10	1121	162
AICH04	34.9319	137.0568	5	241	433
AICH05	34.8886	136.8763	50	301	1051
AICH06	34.6158	137.0419	5	219	85
AICH07	35.2194	137.4039	621	428	50
AICH08	34.9189	137.2993	90	449	50
AICH09	34.6643	137.3902	60	274	342
AICH18	34.9635	137.2377	200	499	10
AICH19	34.9512	137.4114	545	587	32
AICH20	34.8976	137.4876	55	691	54
AICH21	34.7401	136.9385	20	355	50
AICH22	34.7853	137.4393	30	405	132
AICH23	34.8806	136.8316	3	**202**	**1045**
JMA925	35.1532	136.7285	-1	**143**	**1377**
JMA926	34.7149	136.9285	21	343	50
Site name	**Latitude**	**Longitude**	**Altitude[m]**	**Vs30[m/s]**	**Z1.4[m]**
JMA927	34.8116	137.0304	1	215	387
JMA928	34.9316	137.5737	66	358	37
JMABD7	35.3013	136.8434	10	**227**	**547**
JMAE34	35.1682	136.9654	36	349	550
JMANAG	35.1682	136.9654	36	349	550
JMACD1	35.2682	137.2537	599	882	17
JMA544	34.7566	137.407	15	328	202
JMA545	35.0866	137.1501	41	275	219
JMA546	34.9533	137.1787	26	339	185
JMAE44	34.86	136.8134	3	**217**	**1281**
JMAE45	34.63	137.0934	7	333	153
JMABD6	34.9149	137.507	71	574	46
JMACD2	34.6347	137.1401	33	332	187
JMA547	34.8866	136.8321	3	266	1042
SZO011	35.2128	138.6016	204	474	285
SZO012	35.1271	138.6213	10	419	266
SZO013	35.041	138.476	11	**136**	**560**
SZO014	34.9649	138.3735	19	430	183
SZO015	35.2435	138.3407	452	538	46
SZO016	34.8566	138.3113	3	**246**	**1657**
SZO017	34.6374	138.1281	9	363	546
SZO018	34.7402	138.2241	4	387	1344
SZO019	34.7699	137.9981	37	960	745
SZO020	34.9394	138.076	270	373	63

Table 2 (continued)

Site name	Latitude	Longitude	Altitude[m]	Vs30[m/s]	Z1.4[m]
SZO021	35.0969	138.1332	441	635	6
SZO022	35.0916	137.8136	136	385	30
SZO023	34.8738	137.8164	46	303	114
SZO024	34.7102	137.7197	29	467	787
SZO025	34.7194	137.5314	4	201	291
SZO026	34.9816	137.8975	133	489	35
SZOH24	34.8343	137.6616	19	1126	209
SZOH25	34.6913	137.5604	6	332	327
SZOH26	34.7948	137.9034	23	294	636
SZOH28	34.6683	137.7441	5	**208**	**1031**
SZOH29	35.307	138.1973	880	520	6
SZOH30	35.2233	137.9181	540	506	6
Site name	**Latitude**	**Longitude**	**Altitude[m]**	**Vs30[m/s]**	**Z1.4[m]**
SZOH31	34.9398	138.0767	145	398	59
SZOH32	35.0086	137.8409	325	579	15
SZOH33	35.0146	138.3526	50	520	248
SZOH34	35.1304	138.4243	540	430	175
SZOH36	34.9142	138.2008	90	677	30
SZOH37	35.2028	138.5659	80	366	226
SZOH43	34.9739	138.4924	20	323	331
SZOH53	34.8768	138.0174	182	808	291
JMA540	34.8366	138.1769	59	352	150
JMA541	34.7497	137.9236	10	308	614
JMA542	35.223	138.6199	132	374	303
JMA543	35.0166	138.4852	2	252	548
JMA923	34.94	138.0753	145	428	59
JMA924	34.8033	137.5553	5	287	106
JMABD5	34.7514	137.985	76	409	693
JMACC3	34.6783	138.1833	104	349	595
JMAD2B	34.8597	137.7184	185	500	771
JMAE46	34.7533	137.7117	47	372	523
JMAE47	34.605	138.2136	46	432	594
JMAE48	34.9764	138.4033	14	205	230
JMAHMM	34.7097	137.72	30	271	787
JMAOMA	34.6067	138.2103	47	401	602
JMASHZ	34.9764	138.4033	14	205	230

Sites with Vs30 and Z1.4 written in bold mean the sites with the basin conditions (Vs30 < 250 m/s and Z1.4 > 500 m)

circles show the PGA and PGV at each site, respectively. The black line shows the empirical relationship from Morikawa and Fujiwara (2013), and the black dotted lines show the average plus/minus one standard deviation. This model, with a constant slip value and a constant rupture velocity, yields strong-motion synthetics with PGAs that correspond to the empirical relationship, but the PGVs are slightly lower than the empirical relationship at sites near the hypocenter. At MIE016, the Fourier spectra are about half of the one in CASE-VScr within 0.3–0.4 Hz, where the difference between them is the most significant. The response spectra were slightly smaller for CASE-CScr in almost every period band, with the smallest being approximately one-half to two-thirds that of CASE-VScr at 0.4 to 0.5 s. Because we omitted the acceleration waveform plots for CASE-CScr and CASE-VSvr owing to the difficulty in observing the difference, we added a list of PGA values as Table 3.

Figure 14 shows the Fourier and response spectra at MIE016 for CASE–CScr (solid lines) and CASE-VScr

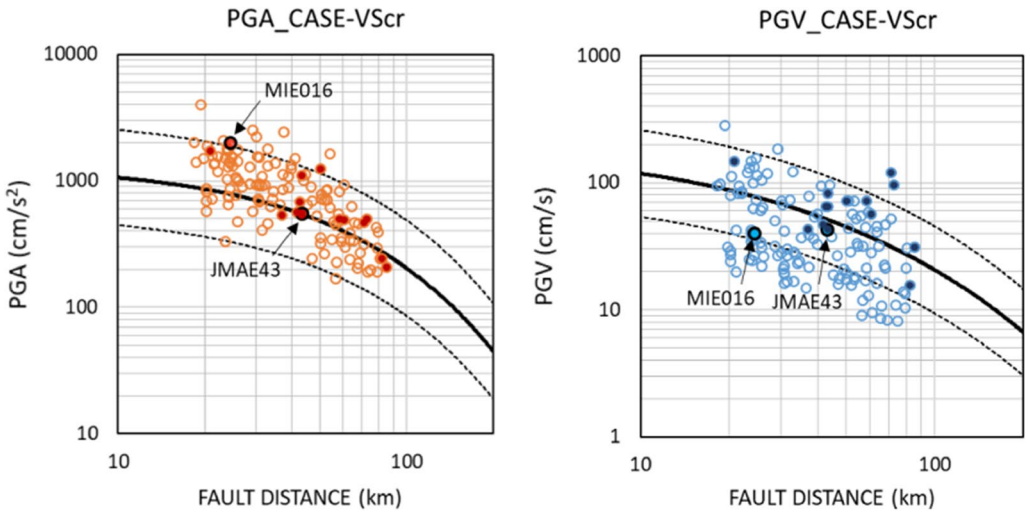

Fig. 8 Attenuation characteristics of PGAs (left) and PGVs (right) in CASE-VScr, together with the GMPEs for PGA and PGV with their standard deviation values derived from the Japanese strong-motion data by Morikawa and Fujiwara (2013). The horizontal axis is the minimum distance from the fault plane, and the vertical axis is PGA or PGV of the value of the vector composite of the two horizontal components. Sites with basin features (namely, Vs30 < 250 m/s and Z1.4 > 500 m) are plotted with small sold circles

(dotted lines). We do not show the results for JMAE43. The systematic differences between CASE-VScr and CASE-CScr were observed; the amplitudes of CASE-CScr are almost always smaller than those of CASE-VScr in the frequency range below 2 Hz (above 0.5 s in period). Direct comparisons of the PGAs and PGVs are presented later in the discussion section.

Model with variable slip and variable rupture velocity (CASE-VSvr)

Figure 15 shows the attenuation relationships of the PGAs and PGVs in CASE-VSvr. The symbols and lines are the same as those in Fig. 13. Figure 16 shows the Fourier and response spectra at MIE016 in Fig. 14 for both CASE-VSvr (solid lines) and CASE-VScr (dotted lines). We do not show the results for JMAE43. A model with variable slip and rupture velocity (CASE-VSvr) yields strong-motion synthetics with PGAs and PGVs that correspond well with the empirical relationship. In the Fourier spectra, although there were some differences in the frequency range lower than 1 Hz, they were at the same level on average. The response spectra also differed in the long-period range. However, the difference between CASE-VSvr and CASE-VScr is not systematic; at one period in one component CASE-VSvr is larger and at another period in another component CASE-VScr is larger. The difference in the shorter period range is marginal. Therefore, it can be said that the overall levels of Fourier and response spectra were similar to each other. Direct comparisons of the PGAs and PGVs are presented later in the Discussion section.

Discussion

Effects of slip variation on PGA and PGV

As shown in previous sections, there is a relatively small difference between the simulated synthetics from CASE-VScr and those from CASE-CScr at a selected site (MIE016) near the hypocenter. This difference reflects the effect of the slip variation on the fault. We need to check whether this is a universal observation at all the analyzed sites.

Figure 17 shows comparisons of the PGAs and PGVs at all sites in the Tokai area. The PGAs from the model with spatial slip variations (CASE-VScr) tended to be slightly higher than the PGAs from the model without spatial slip variations (CASE-CScr). For a smooth slip model (CASE-CScr), we observed a 23% reduction in the PGA compared with a variable slip model (CASE-VScr) based on the regression coefficient of their ratios, 0.77. However, the PGVs from the model with spatial slip variations (CASE-VScr) tended to be higher than the PGVs from the model without spatial slip variations (CASE-CScr). For a smooth-slip model (CASE-CScr), we observed approximately 29% reduction in PGVs in comparison with a variable-slip model (CASE-VScr) based on the regression coefficient of their ratios, 0.71.

These observations may be attributed to the fact that the PGA is the result of random superposition of acceleration waves from each element source, so that it is difficult to see the effects by the slip variations in individual elements with the size of 5 km × 5 km, whereas the PGV is controlled in the intermediate frequency component (0.5 to 5 Hz) so that coherent interferences of waves

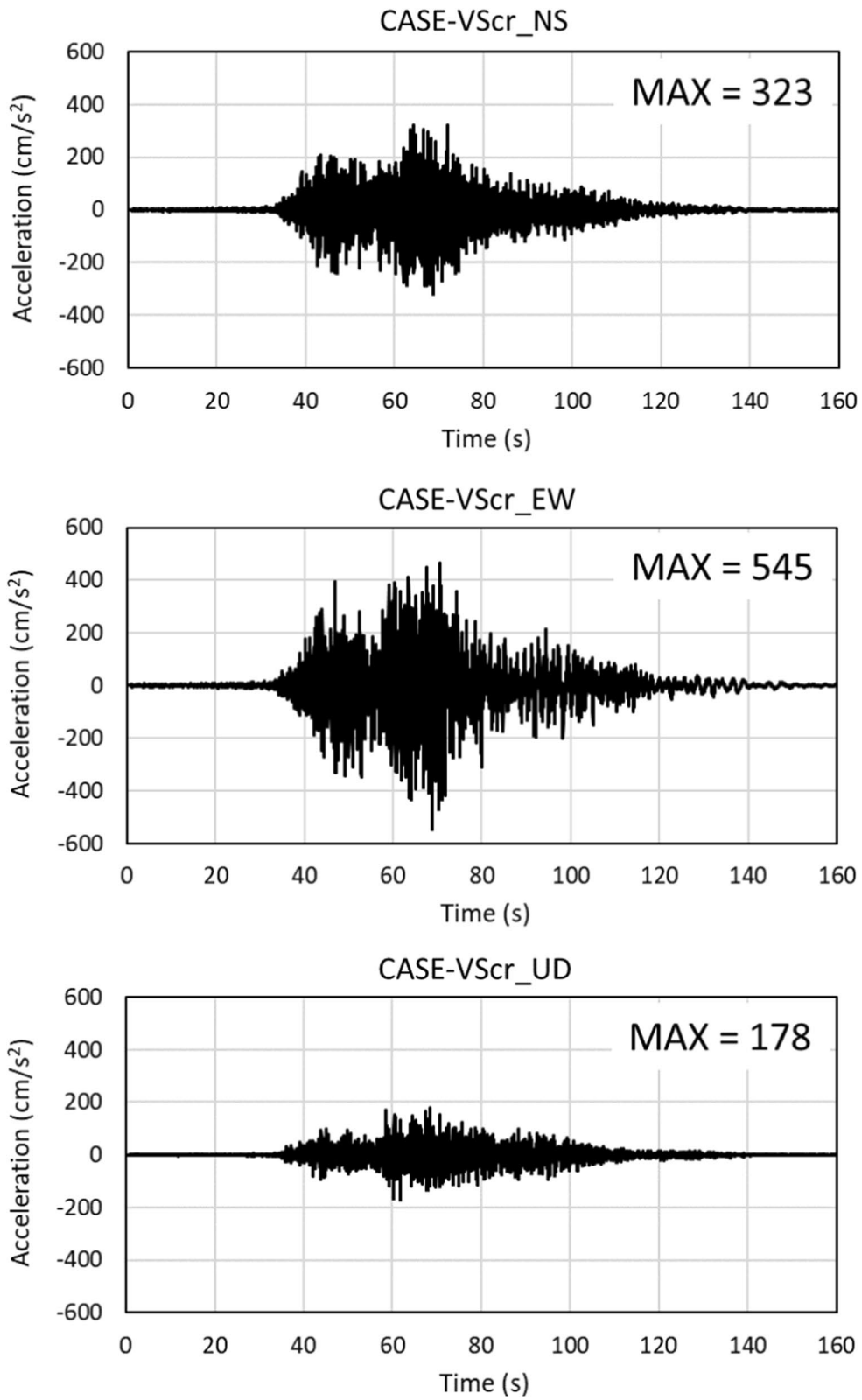

Fig. 9 Acceleration waveforms at JMAE43 in CASE-VScr

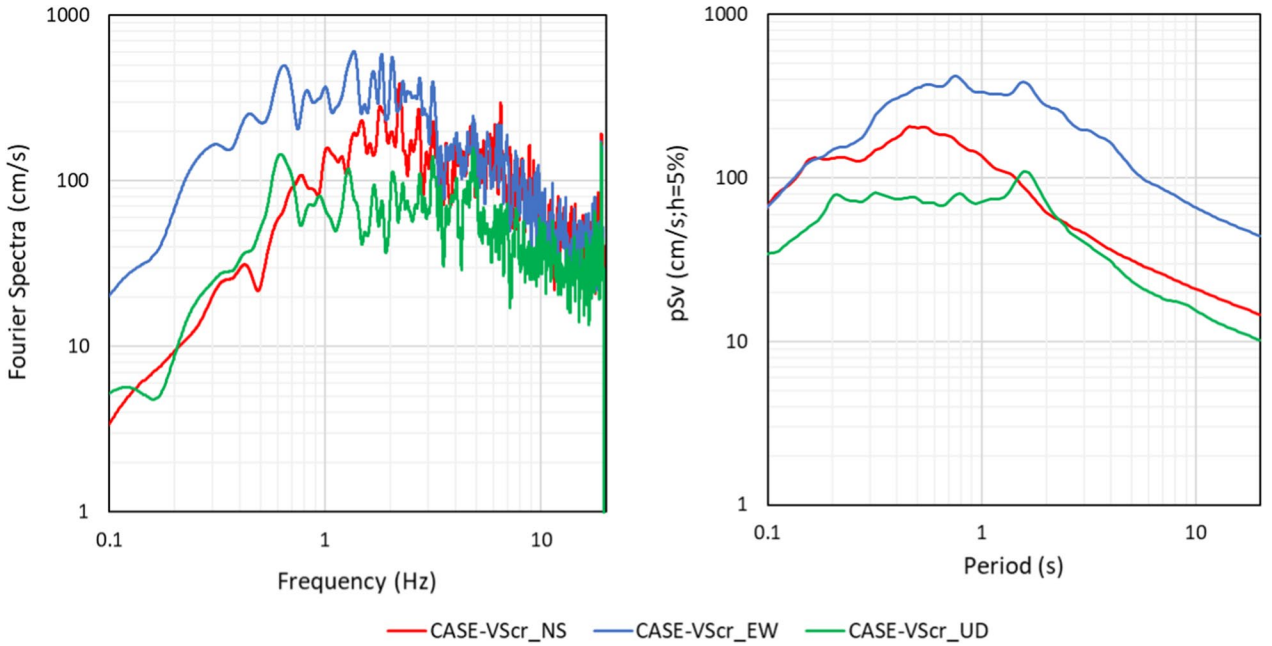

Fig. 10 Acceleration Fourier spectra and pseudo velocity response spectra at JMAE43 in CASE-VScr

from different element sources are taking place. In our simulations, we did not assume any spatial fluctuation in the stress drop in the element sources (except for the SMGAs), which controlled the high-frequency radiation level without slip fluctuation. In the future, it may be necessary to consider the spatial fluctuation of the stress drop to understand how it affects the high-frequency range of the synthetic waveforms.

Effects of rupture velocity variation on PGA and PGV

As shown in previous sections, we can observe a minor effect between the simulated synthetics from CASE-VScr and those from CASE-VSvr at a selected site near the hypocenter. This difference reflects the effect of rupture velocity variation on the fault. We need to check whether this is a universal observation at all sites analyzed.

Figure 18 shows the comparisons of PGAs and PGVs for CASE-VScr and CASE-VSvr at all sites in the Tokai area. Clearly, both the PGAs and PGVs show an almost 1:1 correspondence. The stability of the results in PGAs and PGVs between CASE-VScr and CASE-VSvr could be because of the random phase component introduced in the element source waveforms, which may prevent the possibility of coherent summation of waves, even for the case with a constant rupture velocity.

These values inevitably fluctuate from site to site, even for the same parameter case, because we included site-specific amplification factors that differ significantly from site to site, as shown in Figs. 1 and 2.

Effects of nonlinearity on PGA and PGV

As per the simulation results for CASE-VScr (Figs. 9 and 10 for JMAE43), there are high PGV areas inside the Ise Plain, where strong site amplification is observed in the lower frequency range. When a strong input of seismic motion impinges on thick, soft sediments, soil nonlinearity occurs, and we will have a smaller amplitude in the site amplification factor than the linear one (i.e., amplitude degradation) and a peak frequency shift. Nakano and Kawase (2021) proposed a method using only amplitude degradation, without considering the peak frequency shift. In this report, we consider only amplitude degradation for simplicity.

The amplitude degradation curve proposed by Nakano and Kawase (2021) was based on 174 high PGA and PGV records, together with the Vs30 values at their observation sites. The method follows the one proposed by Yamaguchi and Midorikawa (2014), in which the pseudo-effective shear strain γ'_{eff} is defined as:

$$\gamma'_{eff} = 0.4 \cdot \mathrm{PGV}/Vs30 \tag{10}$$

Then the spectral amplitude degradation $G'(f)$ is modeled as:

$$G'(f) = \alpha\left(f, \gamma'_{eff}\right) \tag{11}$$

$$log_{10}\alpha\left(f, \gamma'_{eff}\right) = a(f) \times \left(log_{10}\gamma'_{eff} - log_{10}\gamma'_{eff\_0}\right) \tag{12}$$

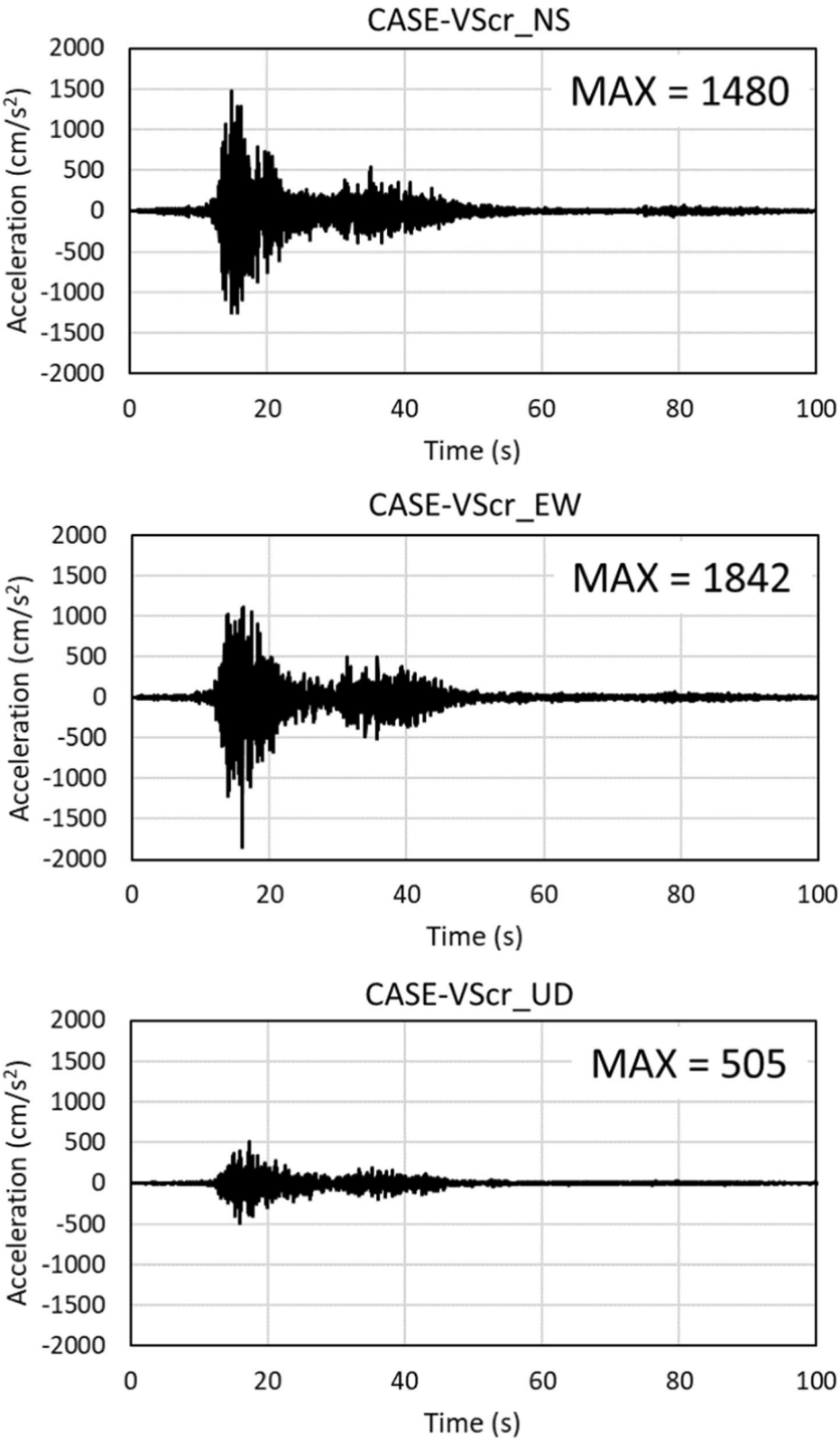

Fig. 11 Acceleration waveforms at MIE016 in CASE-VScr

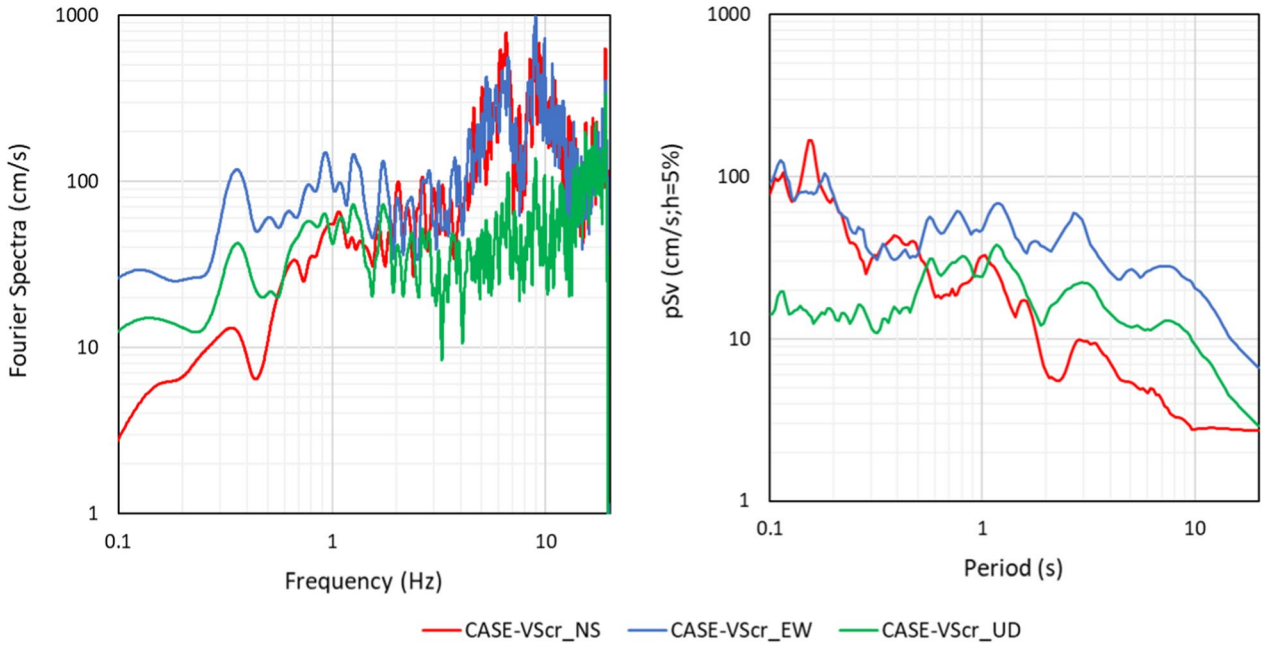

Fig. 12 Acceleration Fourier spectra and pseudo velocity response spectra at MIE016 in CASE-VScr

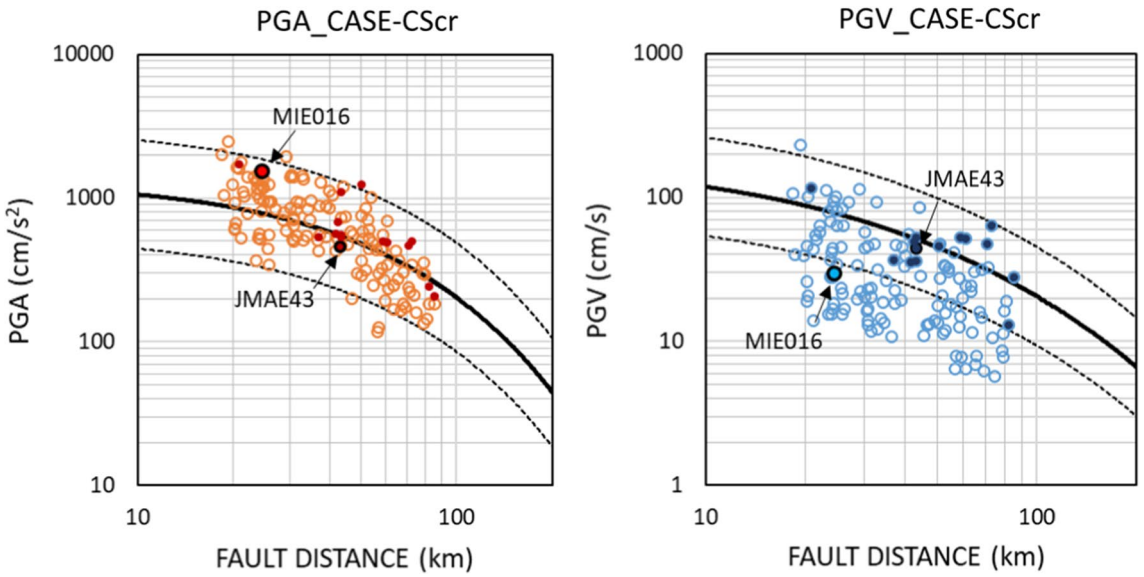

Fig. 13 Attenuation characteristics of PGAs (left) and PGVs (right) in CASE-CScr, together with the GMPEs for PGA and PGV with their standard deviation values (after Morikawa and Fujiwara 2013). Sites with basin features (namely, Vs30 < 250 m/s and Z1.4 > 500 m) are plotted with small sold circles

in which *a(f)* is the regression coefficient for each frequency using a linear function with respect to the excess strain between γ'_{eff} and γ'_{eff_0}, where $\gamma'_{eff\_0}=3.0\times10^{-4}$ is the threshold strain level of the linear regime assumed a priori. Two examples of the initial regression for *a(f)* are shown in the top panels of Fig. 19, whereas the final regression curve *a(f)* as a function of frequency is shown in the bottom panel of Fig. 19. The regression curve was plotted here not as a function of frequency but period $T=1/f$ for comparison with Yamaguchi and Midorikawa (2014). Nonlinearity emerged as a stronger amplitude degradation in the frequency range 1–10 Hz.

Table 3 PGA and PGV values for three cases at JMAE43 and MIE016

Site name	Case name	PGA			PGV		
		NS [cm/s^2]	EW [cm/s^2]	UD [cm/s^2]	NS [cm/s]	EW [cm/s]	UD [cm/s]
JMAE43	CASE-VScr	323	545	178	21	42	13
	CASE-CScr	373	391	154	19	44	11
	CASE-VSvr	441	616	201	27	52	14
MIE016	CASE-VScr	1480	1842	505	30	31	10
	CASE-CScr	1266	1376	482	24	26	9
	CASE-VSvr	1568	1067	590	30	29	14

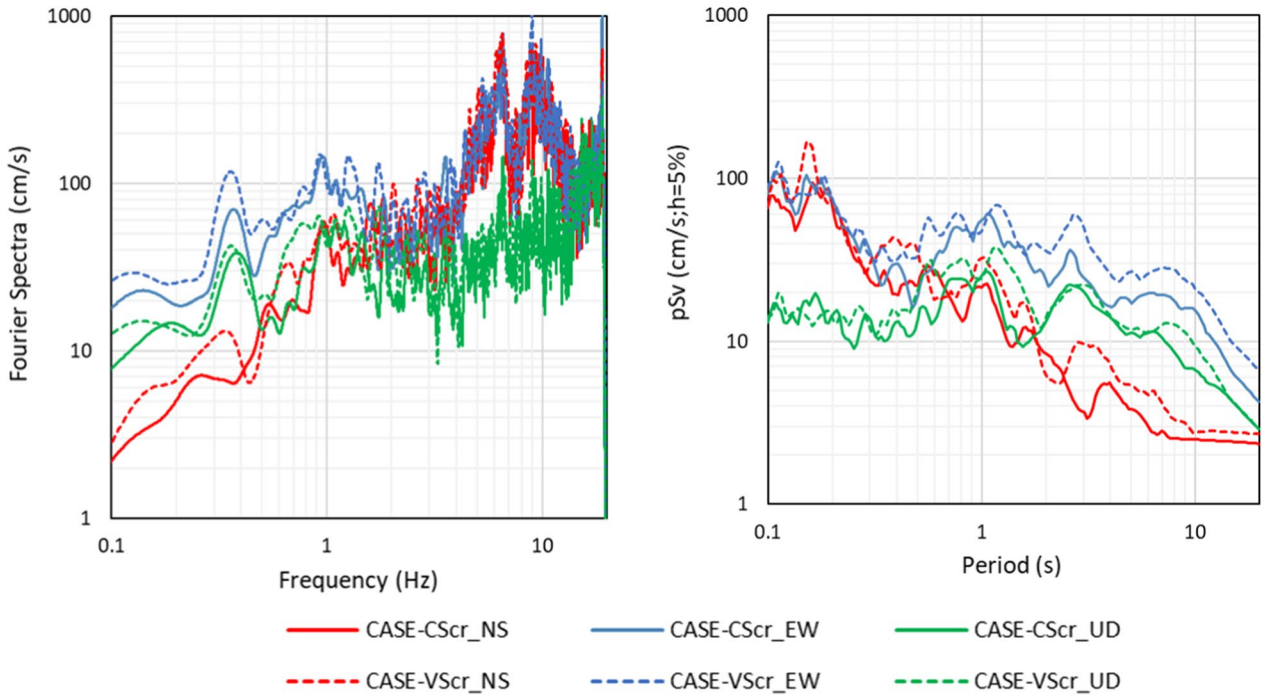

Fig. 14 Acceleration Fourier spectra and pseudo velocity response spectra at MIE016 in CASE-CScr, together with those in CASE-VScr

Figure 20 shows the comparisons of the PGAs and PGVs for CASE-VScr and CASE-VScrNL calculated using the spectral nonlinearity shown in the above formula in addition to the synthetics calculated under the same assumption as CASE-VScr at all sites in the Tokai area. In this figure, the PGAs and PGVs at sites where the PGVs were over 40 cm/s are shown as red circles. From this figure, it can be deduced that the degree of nonlinearity is proportional to the PGV value, which is also evident from Eq. (8) for the same Vs30. The threshold value in terms of the PGV is 40 cm/s. Therefore, the PGAs at sites where the PGVs are over 40 cm/s are clearly affected by nonlinearity, while the PGAs at sites where the PGVs are under 40 cm/s remain the same as in the linear regime. It is also obvious that the effect of nonlinearity on the PGAs for sites with PGV > 40 cm/s tends to be larger than the effect of nonlinearity on the PGVs. This is because PGVs are primarily controlled by the intermediate frequency range from 0.5 Hz to 5 Hz, while PGAs are controlled by the whole frequency range of accelerograms.

It is worth mentioning that the sites with high PGAs near the hypocenter did not show any significant reduction in their Fourier spectra, as shown in Fig. 21, for MIE016 as an example. This is because the effective shear strains in Eq. (8) at these sites were not very large owing to their smaller PGVs and larger Vs30.

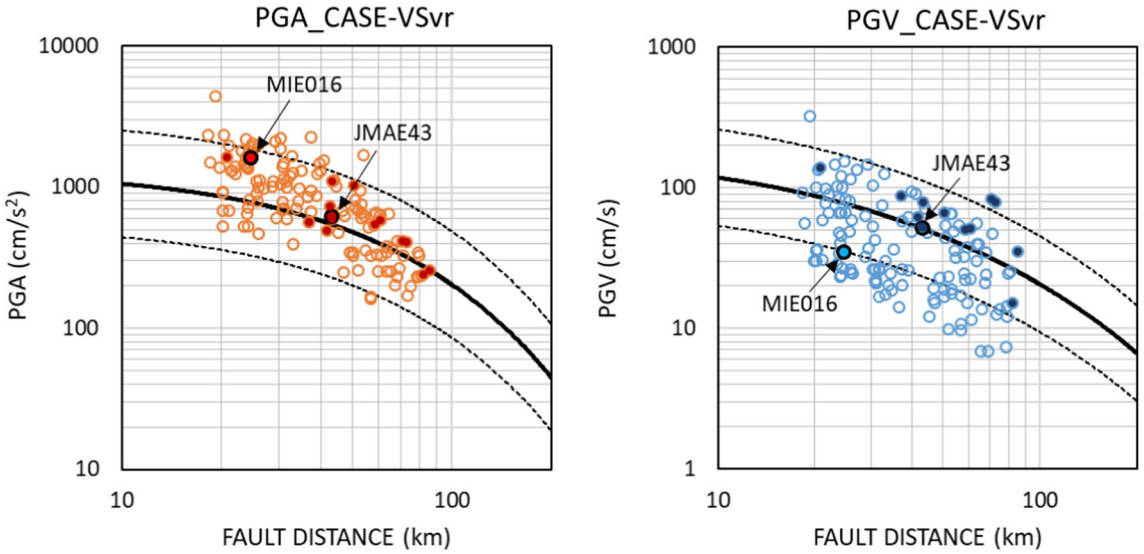

Fig. 15 Attenuation characteristics of PGAs (left) and PGVs (right) in CASE-VSvr, together with the GMPEs for PGA and PGV with their standard deviation values (after Morikawa and Fujiwara 2013). Sites with basin features (namely, Vs30 < 250 m/s and Z1.4 > 500 m) are plotted with small sold circles

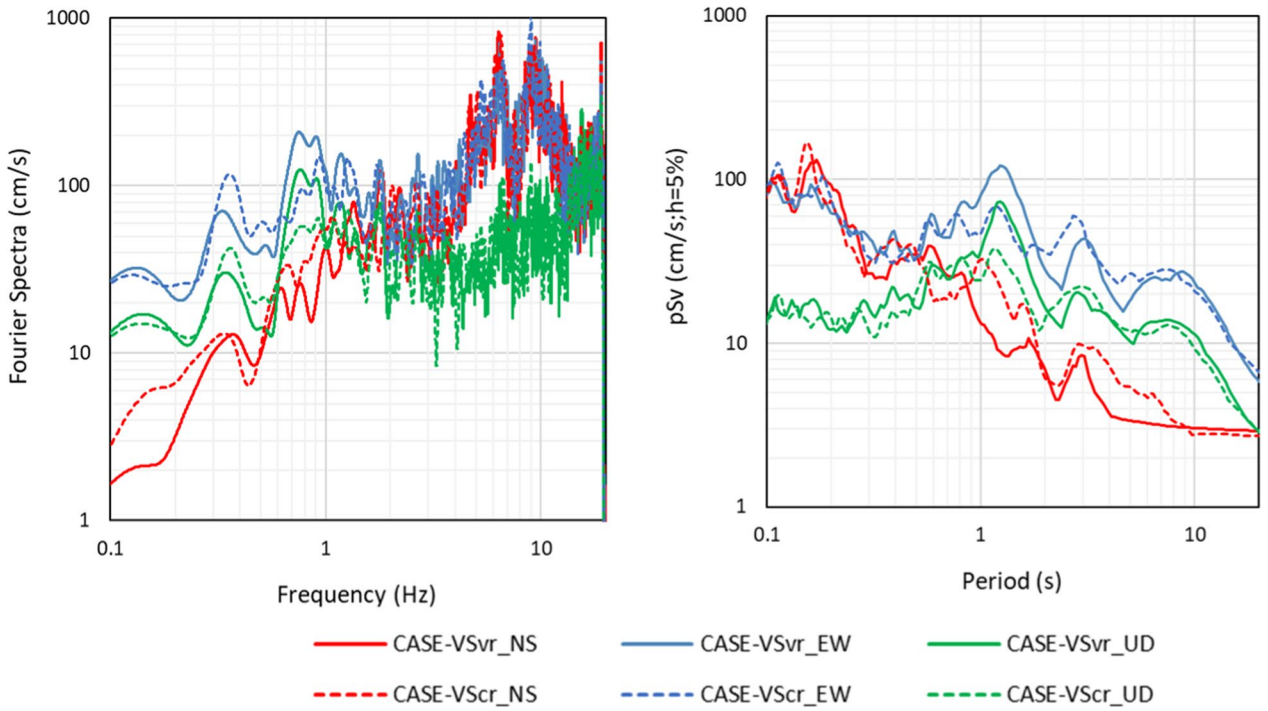

Fig. 16 Acceleration Fourier spectra and pseudo velocity response spectra at MIE016 in CASE-VSvr, together with those in CASE-VScr

Considering these fundamental characteristics of the resultant soil nonlinearity, we believe that the empirical approach for soil nonlinearity correction adopted in the current implementation will be useful for the large-scale prediction of strong motions as a first-order approximation. Please note that the discrepancy between the synthetics and GMPE will increase inevitably by considering the nonlinearity, which is natural as the current synthetic PGA matches to the GMPE. Further validation of the empirical method to consider nonlinearity is needed.

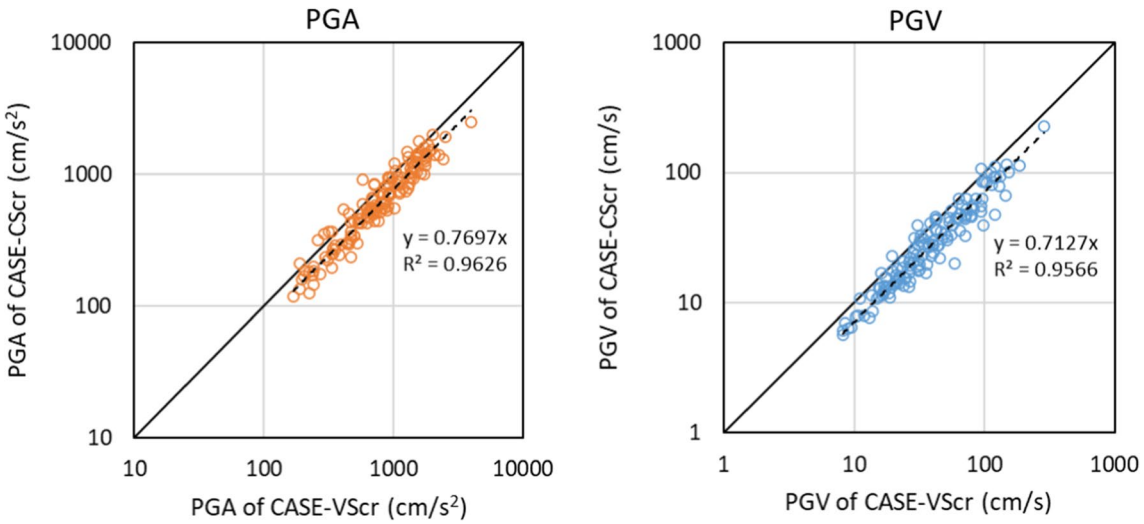

Fig. 17 Comparisons of PGAs and PGVs for the calculated synthetics of CASE-VScr and CASE-CScr. CASE-VScr is the case with slip variations but without rupture velocity variations, and CASE-CScr is the case without both slip variations and rupture velocity variations. Linear regression lines are plotted in both figures to obtain the average ratios between them

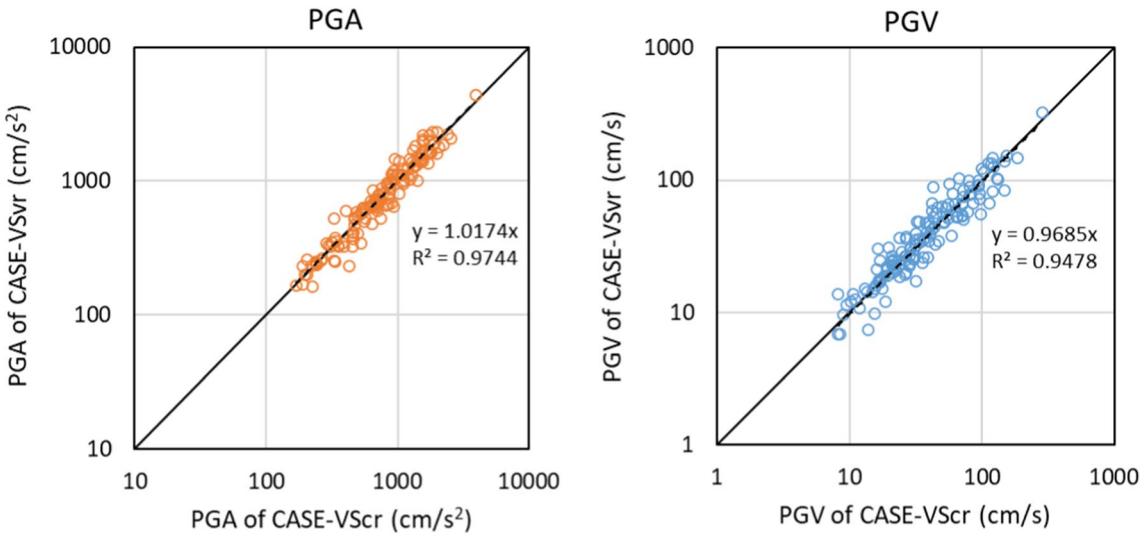

Fig. 18 Comparisons of PGAs and PGVs for the calculated synthetics of CASE-VScr and CASE-VSvr. CASE-VScr is the case slip variations but without rupture velocity variations, and CASE-VSvr is the case with both slip variations and rupture velocity variations. Linear regression lines are plotted in both figures to obtain the average ratios between them

Conclusions

We planned to clarify the source processes of past megathrust earthquakes, the ground motions of which have not been recorded, by adapting the simulated strong-motion waveforms to the results of the damage survey. For realistic strong-motion synthetics, we introduced random spatial heterogeneity in both the slip and rupture propagation velocities in addition to the presumed strong-motion generation areas. We have developed an effective method to predict strong ground motions over a wide frequency range from 0.1 to 20 Hz by combining a randomized source model that can represent complex rupture process on the fault and a statistical Green's function that reflects the statistical properties of small to medium-sized earthquakes extracted from a large number of strong-motion observation records in Japan. The method was applied to the 1944 Tonankai earthquake, and a parametric analysis was performed to investigate the effects of fluctuations in slip and rupture propagation velocities. The main results are summarized as follows.

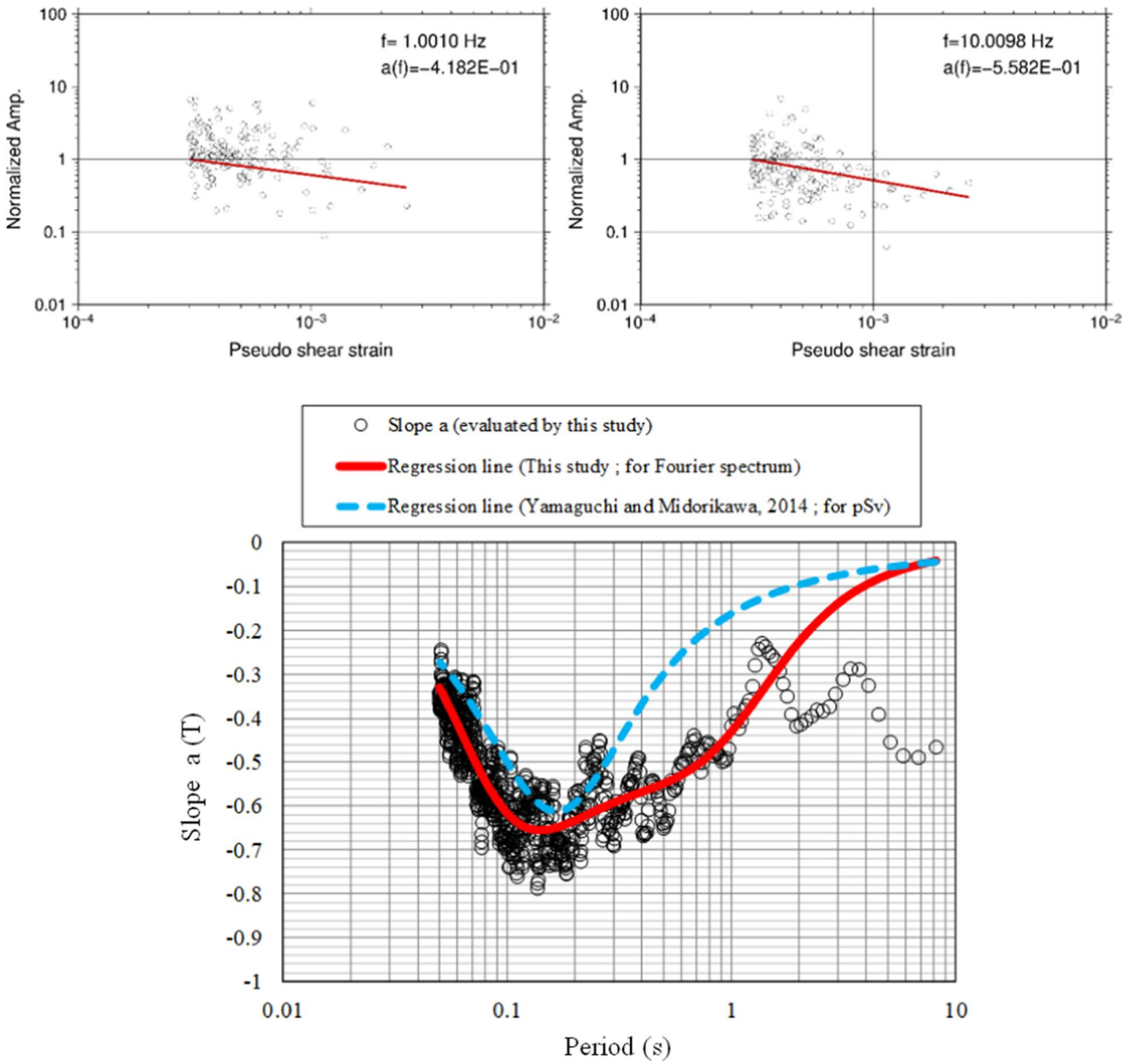

Fig. 19 Examples of the regression procedure for the amplitude degradation as a function of the effective shear strain (PGV/Vs30) at 1 Hz and 10 Hz (top) and the resultant regression coefficients of nonlinearity as a function of period (reciprocal of frequency) applicable to the site term in the form of Fourier spectra (bottom). Open circles in the latter figure are regression coefficients for individual periods as shown in the top panels, while the red curve is derived from their smoothed average. For comparison, the same regression coefficients for the pseudo-velocity response spectra (pSv) by Yamaguchi and Midorikawa (2014) were also plotted (blue broken line)

1) The standard model with random slip fluctuation without rupture velocity perturbation (CASE-VScr), a model with constant slip and constant rupture velocity (CASE-CScr), and a model with both random slip fluctuation and variable rupture velocity (CASE-VSvr) yield strong-motion synthetics with both PGAs and PGVs corresponding to the empirical relationship. The PGVs in CASE-CScr were underestimated compared with those in CASE-VScr and CASE-VSvr because CASE-CScr has a constant slip value and rupture velocity. The introduction of fluctuations in the slip values under the current model resulted in an increase in the PGA by 23% and PGV by 29%.
2) The variations in the rupture propagation velocity had no significant effects on either the PGA or PGV, probably because of the stochastic nature of the statistical Green's function method adopted here.

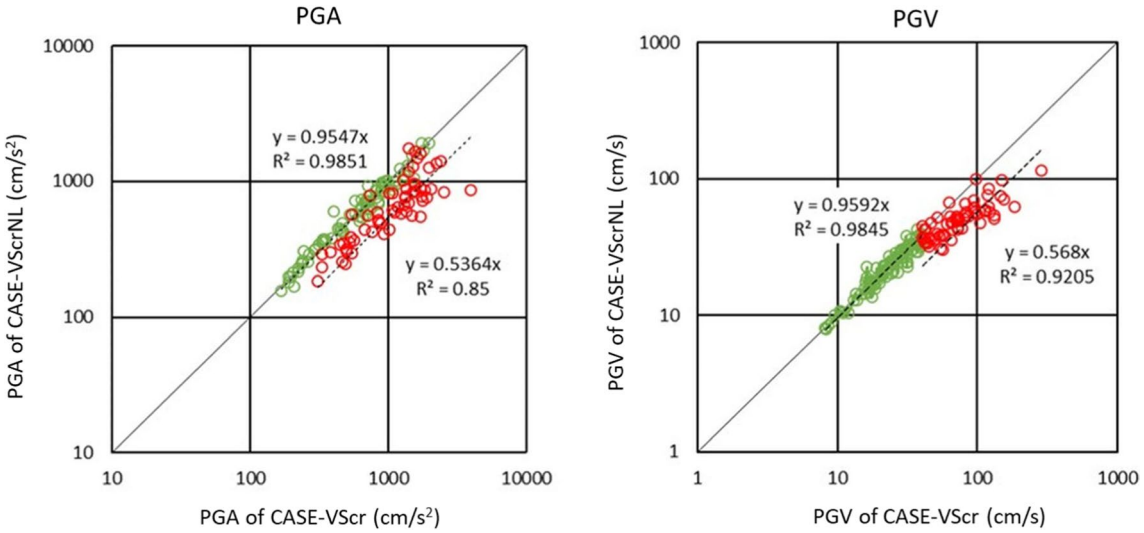

Fig. 20 Comparisons of PGAs and PGVs for the calculated synthetics of CASE-VScr with those of CASE-VScrNL. For both of PGAs and PGVs, the sites where the PGVs are over 40 cm/s are shown in red circles. Linear regression lines are plotted in both figures, separated with the PGV ranges

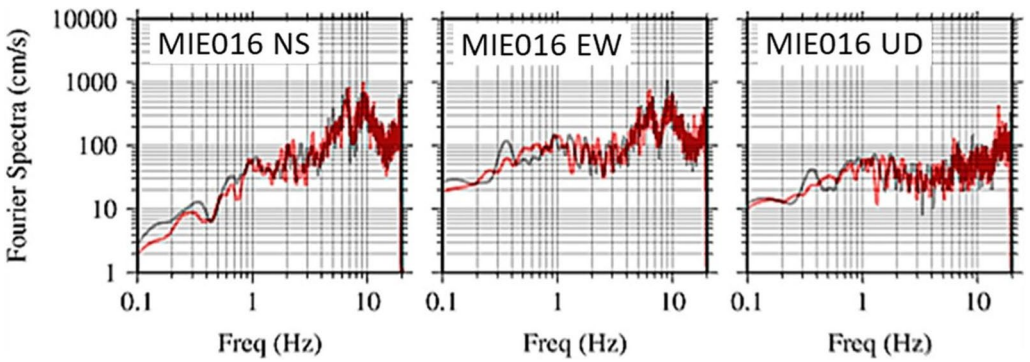

Fig. 21 Comparison of acceleration Fourier spectra of CASE-VScr without considering nonlinearity with those of CASE-VScrNL with considering nonlinearity at MIE016. The Fourier spectra of CASE-VScr is in black line, and those of CASE-VScrNL is in red line

3) The proposed empirically modelled nonlinearity, which considers a strong amplitude degradation in the frequency range from 1 to 10 Hz, reduces both PGAs and PGVs at sites with higher PGVs and smaller Vs30. However, the degree of nonlinearity is larger in PGAs than in PGVs. This is because the PGA is controlled over a broader frequency range than the PGV.

As for the overall characteristics of the calculated synthetics, we found that our current implementation of the complex source model used as a broadband kinematic source representation and the empirically obtained statistical Green's function used as an element source of strong motions can be a viable combination for broadband (0.1 to 20 Hz) strong-motion simulations, realistic in terms of the amplitude and duration, without any hybrid scheme.

In the future, we will estimate building damage ratios by inputting the acceleration waveforms into the wooden building model with construction age and then search for the most realistic source rupture model through a large number of parametric analyses until the estimated damage ratio at each site matches the observed one.

Abbreviations

CDMC	The Central Disaster Management Council
EGF	The empirical Green's function method
eHVSR	The earthquake horizontal-to-vertical spectral ratio
GIT	The generalized spectral inversion technique
GMPE	Ground-motion prediction equation
GMT	Generic mapping tools
HSAF	Horizontal site amplification factor
JIVSM	The Japan Integrated Velocity Structure Model

JMA	Japan meteorological agency
J-SHIS	Japan seismic hazard information station
PGA	Peak ground acceleration
PGV	Peak ground velocity
pSv	Pseudo-velocity response spectra
SCEC	Southern California Earthquake Center
SGF	Statistical Green's function method
SMGA	Strong-motion-generation areas
2D/3D	Two dimensional/three dimensional
VSAF	Vertical site amplification factor
Vs30	The time-averaged S-wave velocity of top 30 m
WSR	The whole-wave-to-S-wave ratio

Acknowledgements
Some of the figures were created using GMT (Wessel et al., 2013). A satellite image from Google Maps is shown in Fig. 1. We used strong-motion records observed in the JMA Shindokei network, K-NET, and KiK-net (NIED, 2019).

Author contributions
Statistical Green's function from the GIT was provided by KN, and waveform synthetic calculations were performed by EI with instructions from KN. The stochastic source model was constructed by EI using the code provided by HS. A parametric study of the source models and their analyses were performed by EI, HK, and NF through discussions with KN and HS. All the authors contributed to the editing and revision of the manuscript. All the authors have read and approved the final version of the manuscript. All authors read and approved the final manuscript.

Funding
This work was partially supported by KAKENHI 21K14388.

Availability of data and materials
All data generated or analyzed in this study are included in the published article. Digital data are available upon request from the corresponding author.

Declarations

Ethics approval and consent to participate
Not applicable.

Consent for publication
All authors have agreed to the publication of the manuscript.

Competing interests
The authors declare that they have no competing interests.

Author details
[1]DPRI, Kyoto University, Gokasho, Uji, Japan. [2]HAZAMA-ANDO CORP, Karima, Tsukuba 515-1, Japan.

Received: 3 August 2022 Accepted: 3 May 2023
Published online: 15 June 2023

References

Aki K (1979) Characterization of barriers on an earthquake fault. J Geophys Res 84:6140–6148
Ando M (1975) Source mechanisms and tectonic significance of historical earthquakes along the Nankai trough, Japan. Tectonophysics 27:119–140
Andrews DJ (1986) Objective determination of source parameters and similarity of earthquakes of different size. In: Das S, Boatwright J, Scholz CH (eds) Earthquake source mechanics. American Geophysical Union, Washington
Asano K, Iwata T (2012) Source model for strong ground motion generation in the frequency range 0.1–10 Hz during the 2011 Tohoku earthquake. Earth Planets Space 64:1111–1123. https://doi.org/10.5047/eps.2012.05.003
Baoyintu, Mandula N, Kawase H, Mantegeer B, Bao Y. Broadband statistical Green's functions based on observed data by strong motion networks and its application to Tonankai earthquake, in Intelligent Systems and Decision Making for Risk Analysis and Crisis Response (Eds. Chongfu Huang and Cengiz Kahraman), Proceedings of the 4th International Conference on Risk Analysis and Crisis Response, Istanbul, Turkey, 27–29 August 2013; 293–300, CRC Press, London. Doi: https://doi.org/10.1201/b16038
Baoyintu MN, Kawase H (2021) Broadband strong-motion prediction for future Nankai-Trough earthquakes using statistical Green's function method and subsequent building damage evaluation. Appl Sci 11(15):7041. https://doi.org/10.3390/app11157041
Bard P-Y, Bouchon M (1980) Seismic response of sediment-filled valleys, Part 1: the case of incident SH waves. Bull Seismol Soc Am 70:1263–1286
Boore DM (1983) stochastic simulation of high-frequency ground motion based on seismological models of radiated spectra. Bull Seism Soc Am 173:1865–1894
Cabinet Office. Report on long-period ground motion due to a Nankai Trough megaquake, Committee for Modeling a Nankai Trough Megaquake, December 17, 2015. (**in Japanese**) http://www.bousai.go.jp/jishin/nankai/ nankaitrough_report.html, Accessed 10 Jun 2022
Central Disaster Management Council. Strong motions and Tsunami heights, Figures and Tables, Vol.3. 2003. (**in Japanese**) https://www.bousai.go.jp/kaigirep/chuobou/senmon/tounankai_nankaijishin/16/pdf/siryou3zuhyou_2.pdf, Accessed 10 Jun 2022.
Das S, Aki K (1977) Fault plane with barriers: A versatile earthquake model. J Geophys Res 82:5658–5670
Graves RW, Pitarka A. Broadband time history simulation using a hybrid approach. In: 13th World Conference on earthquake engineering, Vancouver; 2004. Paper no. 1098.
Graves RW, Pitarka A (2010) Broadband ground-motion simulation using a hybrid approach. Bull Seismol Soc Am 100(5A):2095–2123. https://doi.org/10.1785/0120100057
Graves RW, Pitarka A (2016) Kinematic ground-motion simulations on rough faults including effects of 3D stochastic velocity perturbations. Bull Seismol Soc Am 106(5):2136–2153. https://doi.org/10.1785/0120160088
Guatteri M, Mai PM, Beroza GC, Boatwright J (2003) Strong ground-motion prediction from stochastic-dynamic source models. Bull Seismol Soc Am 93:301–313
Ho N, Kawase H (2007) Broadband stochastic green's functions based on observed data by strong motion networks and its application to Nankai earthquake. J JAEE 7(2):80–95 ((**in Japanese with English abstract**))
Irikura K, Miyake H, Iwata T, Kamae K, Kawabe H, and Dalguer LA. Recipe for predicting strong ground motion from future large earthquake, Proceedings of the 13th World Conference on Earthquake Engineering, 2004.No. 1371 (CD-ROM).
Irikura K, Miyake H (2001) Prediction of strong ground motions for scenario earthquakes. J Geogr 110:849–875 ((**In Japanese with English abstract**))
Irikura K, Miyake H (2011) Recipe for predicting strong ground motion from crustal earthquake scenarios. Pure Appl Geophys 168:85–104. https://doi.org/10.1007/s00024-010-0150-9
Ito E, Nakano K, Nagashima F, Kawase H (2020b) A method to directly estimate S-wave site amplification factor from horizontal-to-vertical spectral ratio of earthquakes (eHVSRs). Bull Seismol Soc Am 110(6):2892–2911. https://doi.org/10.1785/0120190315
Ito E, Nakano K, Sekiguchi H, Kawase H. Strong motion simulation for the 1944 Tonankai earthquake based on the statistical Green's Function method and stochastic representation of complex source process, DPRI Annuals. 2020a; 63B:1–16. https://www.dpri.kyoto-u.ac.jp/nenpo/no63/ronbunB/a63b0p01.pdf.
Itoh S, Kuhara H, Kawase H (2001) Statistical characteristics of seismic ground motions estimated from K-NET records and Green's function synthesis for semi-empirical method. J Struct Constr Eng, AIJ 543:37–44 ((**in Japanese with English abstract**))
Iwata T, Irikura K (1988) Source parameters of the 1983 Japan-Sea earthquake sequence. J Phys Earth 36:155–184
Ji L, Xie X, Pan X (2022) Improvement of stochastic green's function method for 3d broadband ground-motion simulation. Seismol Res Lett 94(1):331–349. https://doi.org/10.1785/0220220010
J-SHIS. Japan Seismic Hazard Information Station, NIED, Tsukuba, Japan. 2020. http://www.j-shis.bosai.go.jp/en/ Accessed 10 Jun 2022.

Kamae K, Irikura K (1995) A fault rupture model of the 1995 Hyogoken Nambu earthquake (MJMA = 7.2) estimated by the empirical Green's function method. J. Natural Disas Sci. 16(2):31–40
Kamae K, Irikura K (1998) Source model of the 1995 Hyogo-ken Nanbu earthquake and simulation of near-source ground motion. Bull Seismol Soc Am 88(2):400–412
Kamae K, Kawabe H (2004) Source model composed of asperities for the 2003 Tokachi-Oki, Japan, earthquake (MJMA=8.0) estimated by the empirical Green's function method. Earth Planets Space 56:323–327. https://doi.org/10.1186/BF03353059
Kanamori H (1981) The nature of seismicity patterns before large earthquakes. In: Simpson DW, Richards PG (eds) Earthquake prediction: an international review. American Geophysical Union, Washington, pp 1–19
Kawase H (2003) Site effects on strong ground motions. In: Lee WHK, Kanamori H (eds) International Handbook of Earthquake and Engineering Seismology, Part B. London, Academic Press, pp 1013–1030
Kawase H, Aki K (1989) A study on the response of a soft basin for incident S P, and Rayleigh Waves with Special Reference to the Long Duration Observed in Mexico City. Bull Seismol Soc Am 79:1361–1382
Kawase H, Sánchez-Sesma FJ, Matsushima S (2011) The optimal use of horizontal-to-vertical spectral ratios of earthquake motions for velocity inversions based on diffuse field theory for plane waves. Bull Seismol Soc Am 101:2001–2014
Kawase H, Matsuo H. Amplification characteristics of K-NET, KiK-NET, and JMA Shindokei network sites based on the spectral inversion technique. In: 13th World Conference on Earthquake Engineering, Vancouver; 2004. Paper No. 454.
Kawase H, Matsushima S, Graves RW, Somervill PG. Strong motion simulation of Hyogo-ken Nanbu (Kobe) earthquake considering both the heterogeneous rupture process and the 3-D basin structure. In:12th World Conference on Earthquake Engineering, Auckland; 2000.CD-ROM Ref. No.990, 1–8
Kikuchi M, Kanamori H (1982) Inversion of complex body waves. Bull Seismol Soc Am 72(2):491–506
Kikuchi M, Kanamori H (1986) Inversion of complex body waves-II. Phys Earth Planet Inter 43:205–222. https://doi.org/10.1016/0031-9201(86)90048-8
Kikuchi M, Kanamori H (1991) Inversion of complex body waves - III. Bull Seismol Soc Am 81:2335–2350
Koketsu K, Miyake H, Suzuki H. Japan integrated velocity structure model version 1. In: 15th world conference on earthquake engineering, Lisbon, Portugal; 2012. Paper No.1773
Kurahashi S, Irikura K (2013) Short-period source model of the 2011 Mw 9.0 off the Pacific coast of Tohoku earthquake. Bull Seismol Soc Am 103:1317–1393
Lay T, Kanamori H (1980) Earthquake doublets in the Solomon Islands. Phys Earth Planet Inter 21(4):283–304. https://doi.org/10.1016/0031-9201(80)90134-x
Lay T, Kanamori H (1981) An asperity model of large earthquake sequences. In: Simpson DW, Richards PG (eds) Earthquake prediction: an international review. American Geophysical Union, Washington, pp 579–592
Lay T, Kanamori H, Ammon CJ, Koper KD, Hutko AR, Ye L, Yue H, Rushing TM (2012) Depth-varying rupture properties of subduction zone megathrust faults. J Geophys Res 117:B04311. https://doi.org/10.1029/2011JB009133
Mai PM, Beroza GC (2002) A spatial random field model to characterize complexity in earthquake slip. J Geophys Res 107(B11):2308. https://doi.org/10.1029/2001JB000588
Miyake H, Iwata T, Irikura K (2003) Source characterization for broadband ground-motion simulation: kinematic heterogeneous source model and strong motion generation area. Bull Seismol Soc Am 93:2531–2545
Miyake H, Murotani S, Koketsu K (2006) Scaling of asperity size for plate-boundary earthquakes. Chikyu Monthly Special Issue 55:86–91 (**(in Japanese)**)
Miyakoshi K, Petukhin A. Delineation of rupture velocity of heterogeneous source model extracted from source inversion results of inland earthquakes. In: 2005 Japan Earth and Planetary Science Joint Meeting, Chiba; 2005.S046P-002.
Miyakoshi K, Kagawa T, Sekiguchi H, Iwata T, Irikura K. Source characterization of inland earthquakes in Japan using source inversion results. In: 12th World Conference on Earthquake Engineering, Auckland; 2000.1850.
Miyakoshi K, Petukhin A, Kagawa T. Source modeling of inland earthquakes for the intermediate period range -Case study of the 1997 Kagoshima-ken Hokuseibu (March) and the 1997 Yamaguchi-ken Hokubu earthquakes-, Fall meeting of Seismological Society of Japan; 2004. P065 (**in Japanese**).
Morikawa N, Fujiwara H (2013) A new ground motion prediction equation for Japan applicable up to M9 mega-earthquake. J Disaster Res 8(5):878–888. https://doi.org/10.20965/jdr.2013.p0878
Nagashima F, Matsushima S, Kawase H, Sánchez-Sesma FJ, Hayakawa T, Satoh T, Oshima M (2014) Application of horizontal-to-vertical (H/V) spectral ratios of earthquake ground motions to identify subsurface structures at and around the K-NET Site in Tohoku Japan. Bull Seismol Soc Am 104(5):2288–2302. https://doi.org/10.1785/0120130219
Nakano K, Kawase H (2019) Source parameters and site amplifications estimated by generalized inversion technique: focusing on the 2018 Hokkaido Iburi-Tobu earthquake. Earth Planets Space 71:66. https://doi.org/10.1186/s40623-019-1047-1
Nakano K, Kawase H (2021) A study on the strong motion prediction method based on the characteristics estimated by generalized inversion technique. J Japan Assoc Earthq Eng 21(2):130–153. https://doi.org/10.5610/jaee.21.2_130. ((**in Japanese with English abstract**))
Nakano K, Matsushima S, Kawase H (2015) Statistical properties of strong ground motions from the generalized spectral inversion of data observed by K-NET, KiK-net, and the JMA Shindokei Network in Japan. Bull Seismol Soc Am 105:2662–2680. https://doi.org/10.1785/0120140349
Nakano K, Kawase H, Matsushima S (2019) A study on the site amplifications estimated by generalized inversion technique. J Japan Assoc Earthq Eng 19(2):1–24. https://doi.org/10.5610/jaee.19.2_1. ((**in Japanese with English abstract**))
National Research Institute for Earth Science and Disaster Resilience. NIED K-NET, KiK-net, National Research Institute for Earth Science and Disaster Resilience. 2019. doi:https://doi.org/10.17598/NIED.0004
Papageorgiou AS, Aki K (1983) A specific barrier model for the quantitative description of inhomogeneous faulting and the prediction of strong ground motion. Part I Description of the model. Bull Seismol Soc Am 73:693–722
Pitarka A, Irikura K (1996) Basin structure effects on long-period strong motions in the San Fernando Valley and the Los Angeles Basin from the 1994 Northridge earthquake and an aftershock. Bull Seismol Soc Am 86:S126–S137
Pitarka A, Graves R, Irikura K, Miyakoshi K, Rodgers A (2020) Kinematic rupture modeling of ground motion from the M7 Kumamoto. Japan Earthquake Pure Appl Geophys 177:2199–2221. https://doi.org/10.1007/s00024-019-02220-5
Renka R (1999) Algorithm 790: CSHEP2D: Cubic Shepard method for bivariate interpolation of scattered data. ACM Trans Math Softw 25(1):70–73. https://doi.org/10.1145/305658.305737
Rodgers A, Petersson NA, Pitarka A, McCallen D, Sjogreen B, Abrahamson N (2019) Broadband (0–5 Hz) fully deterministic three-dimensional ground motion simulations of a magnitude 7.0 Hayward Fault earthquake: Comparison with empirical ground motion models and 3D path and site effects from source normalized intensities. Seismol Res Lett 90(3):1268–1284. https://doi.org/10.1785/0220180261
Sato T, Murono Y, Nishimura A (2002) Phase spectrum modeling to simulate design earthquake motion. J Nat Dis Sci 24(1):91–100
Satoh T (2004) Study on envelope model of ground motions based on inversion of group delay time and scattering theory. J Struct Constr Eng AIJ 586:71–78. https://doi.org/10.3130/aijs.69.71_5. ((**in Japanese with English abstract**))
Sekiguchi H, Yoshimi M (2011) Broadband ground motion reconstruction for the Kanto Basin during the 1923 Kanto earthquake. Pure Appl Geophys 168:609–630. https://doi.org/10.1007/s00024-010-0142-9
Senna S, Wakai A, Yatagai A, Jin K, Matsuyama H, Suzuki H, Fujiwara H. Modeling of the subsurface structure from the seismic bedrock to the ground surface for a broadband strong motion evaluation in Japan. In: Proc of 7th Int Conf Earthq Geotech Eng. Malta, 2019.
Smith FHW, Wessel P (1990) Gridding with continuous curvature splines in tension. Geophysics. https://doi.org/10.1190/1.1442837
Somerville PG, Irikura K, Graves R, Sawada S, Wald D, Abrahamson N, Iwasaki Y, Kagawa T, Smith N, Kowada A (1999) Characterizing crustal earthquake slip models for the prediction of strong ground motion. Seism Res Lett 70:59–80

Takemura M, Toraya K (2015) Re-Evaluation of seismic intensity distribution from the1944 Tonankai earthquake and its disaster characteristics. J Japan Assoc Earthq Eng, Spec Issue. https://doi.org/10.5610/jaee.15.7_2

The Headquarters for Earthquake Research Promotion. List of long-term evaluation results of active faults and subduction plate-boundary earthquakes published to date. 2022. https://www.jishin.go.jp/main/choukihyoka/ichiran.pdf. Accessed 10 Jun 2022.

Wakai A, Senna S, Jin K, Yatagai A, Suzuki H, Inagaki W, Matsuyama H, Fujiwara H (2019) Modeling of subsurface velocity structures from seismic bedrock to ground surface in the Tokai region, Japan, for broadband strong ground motion prediction. J Disaster Res 14(9):1140–1153

Wang Z, Nakano K, Ito E, Kawase H, Matsushima S (2023) A hybrid approach for deriving horizontal site amplification factors considering both the similarity of HVSRe and the vertical amplification correction function. Earthq Eng Struct Dyn 52:128–146. https://doi.org/10.1002/eqe.3753

Wessel P, Smith HFW, Scharroo R, Luis JF, Wobbe F (2013) Generic Mapping tools: improved version released. EOS Trans AGU 94:409–410

Yamaguchi M, Midorikawa S (2014) Empirical models for nonlinear site amplification evaluated from observed strong motion records. J Japan Assoc Earthq Eng 14(1):56–70. https://doi.org/10.5610/jaee.14.1_56. ((**in Japanese with English abstract**))

Publisher's Note